

Unique signatures of Population III stars in the global 21-cm signal

Jordan Mirocha,¹★ Richard H. Mebane,¹ Steven R. Furlanetto,¹ Krishma Singal² and Donald Trinh³

¹*Department of Physics and Astronomy, University of California, Los Angeles, CA 90024, USA*

²*School of Physics, Georgia Institute of Technology, Atlanta, GA 30332, USA*

³*Department of Physics and Astronomy, University of California, Irvine, CA 92697, USA*

Accepted 2018 May 21. Received 2018 April 16; in original form 2017 July 28

ABSTRACT

We investigate the effects of Population III stars on the sky-averaged 21-cm background radiation, which traces the collective emission from all sources of ultraviolet and X-ray photons before reionization is complete. While ultraviolet (UV) photons from Pop III stars can, in principle, shift the onset of radiative coupling of the 21-cm transition – and potentially reionization – to early times, we find that the remnants of Pop III stars are likely to have a more discernible impact on the 21-cm signal than Pop III stars themselves. The X-rays from such sources preferentially heat the intergalactic medium (IGM) at early times, which elongates the epoch of reheating and results in a more gradual transition from an absorption signal to emission. This gradual heating gives rise to broad, asymmetric wings in the absorption signal, which stand in contrast to the relatively sharp, symmetric signals that arise in models treating Pop II sources only. A stronger signature of Pop III, in which the position of the absorption minimum becomes inconsistent with Pop II-only models, requires extreme star-forming events that may not be physically plausible, lending further credence to predictions of relatively high-frequency absorption troughs, $\nu_{\min} \sim 100$ MHz. As a result, though the trough location alone may not be enough to indicate the presence of Pop III, the asymmetric wings should arise even if only a few Pop III stars form in each halo before the transition to Pop II star formation occurs, provided that the Pop III IMF is sufficiently top-heavy and at least some Pop III stars form in binaries.

Key words: galaxies: high-redshift – intergalactic medium – galaxies: luminosity function, mass function – dark ages, reionization, first stars – diffuse radiation.

1 INTRODUCTION

The formation of the first generations of stars in the Universe has been a topic of great interest for several decades (for a recent review, see Bromm 2013). These so-called Population III (Pop III) stars by definition form out of chemically pristine clouds, a fact which is expected to give rise to stellar initial mass functions (Bromm, Coppi & Larson 1999; Abel, Bryan & Norman 2002), atmospheres (Tumlinson & Shull 2000; Bromm, Kudritzki & Loeb 2001; Schaerer 2002), and chemical yields (Heger & Woosley 2002) that are distinct from stars today. Depending on the efficiency with which such stars form in high- z dark matter haloes and their longevity as a population, traces of their existence may be found in the reionization history of the intergalactic medium (IGM) (e.g., Visbal, Haiman & Bryan 2015; Miranda et al. 2017), chemical abundance patterns in metal-poor stars in the Milky Way (e.g., Jeon, Besla & Bromm 2017;

Magg et al. 2018), and pair-instability supernova (PISN) rates at high redshift (e.g., Whalen et al. 2014). As a result, further investigation of the Pop III epoch continues not only due to a fundamental interest in the physical processes that govern star formation, but because progress in so many other areas may be inextricably linked to the lives and deaths of Pop III stars.

Observationally, Pop III stars have remained elusive. This is not surprising, given that they are expected to form in low mass ($\sim 10^5$ – $10^6 M_{\odot}$) dark matter haloes at the highest redshifts, and probably only in small numbers. There has been only one object detected at high- z with some evidence of Pop III-like stellar population (Sobral et al. 2015), though more ordinary explanations remain viable (Bowler et al. 2017), especially after the recent detection of [CII] (Matthee et al. 2017). Similarly, while there have been a few claims of supernovae at $z \sim 3$ whose properties are consistent with pair-instability models, and thus very massive $M \gtrsim 100 M_{\odot}$ supernova progenitors still even after reionization (Cooke et al. 2012), the lack of iron in the most metal-poor nearby stars suggest somewhat less massive progenitors at high- z (Keller et al. 2014).

★ E-mail: mirocha@astro.ucla.edu

Another way to constrain Pop III stars is to compare the ionizing photon density of known sources relative to that needed to maintain an ionized IGM at $z \gtrsim 6$, and/or τ_e values consistent with *Planck*'s latest measurements (e.g., Visbal et al. 2015). If there is a deficit in the measured photon density relative to what is needed, one might invoke new, as-yet-unseen sources of UV photons at high redshift to close the gap. An analogous but more general argument can be made using the global 21-cm signal (Madau, Meiksin & Rees 1997; Shaver et al. 1999; Furlanetto 2006), since the global 21-cm signal is sensitive to the volume-averaged ionized fraction as well as the thermal history of the IGM and Ly- α production histories of galaxies. This was the motivation of Mirocha, Furlanetto & Sun (2017), who established a set of global 21-cm predictions calibrated to measurements of the high- z galaxy luminosity function, and included only ‘normal’ star-forming galaxies in the model. If these models were to be ruled out observationally, it might indicate the presence of unaccounted for source populations like Pop III stars and their remnants.

The ‘deficit elimination’ approach outlined above could provide suggestive evidence of new sources of radiation at high- z . However, apparent deficits can vanish if, for example, we simply do not understand the production and/or escape of photons from normal high- z galaxies. Ideally, new sources would provide some unique signature, other than simply adding to the tally of UV and X-ray photons present at $z \gtrsim 6$.

The zeroth-order expectation is of course that the addition of new source populations will boost the luminosity density relative to the ‘Pop II-only’ predictions of Mirocha et al. (2017), and thus raise the IGM temperature, ionized fraction, and/or mean Ly- α background intensity. However, because the star formation rate density (SFRD) of Pop III stars should be qualitatively different than the SFRD of Pop II stars (e.g., Trenti & Stiavelli 2009; Xu et al. 2016; Mebane, Mirocha & Furlanetto 2017), the boost in luminosity density is likely redshift-dependent. If strong enough, such a z -dependent boost will then manifest as a frequency-dependent modulation of the global 21-cm signal. Our goal in this work is to determine under what circumstances such a modulation can arise, and to determine whether such a signature could be unambiguously associated with Pop III sources (as opposed to, say, uncertainties in the properties of known galaxy populations).

There is certainly no shortage of predictions for the Pop III SFRD in the literature, any one of which we could simply ‘plug-in’ to our 21-cm modelling code. However, if we were to simply adopt Pop III star formation histories (SFHs) from the literature, the self-consistency of our model would likely suffer. As a result, we have devised a new toy model that can give rise to a diverse set of histories that builds naturally from our Pop II-only models (Mirocha et al. 2017). Such a simple model suffices here, as our goal is *not* to try to bring to bear new insights into the physics governing Pop III star formation, but rather to determine the set of Pop III SFHs that leave the most distinct signature in the global 21-cm signal.

Since this paper was submitted, the first reported detection of the global 21-cm signal was announced by the EDGES team (Bowman & Rogers 2010; Bowman et al. 2018). Though the anomalous depth of the signal has garnered much attention, at ~ 78 MHz, its strongest feature is also much earlier than the ~ 100 MHz expectations put forth in Mirocha et al. (2017). A quantitative assessment of the tension between the EDGES measurement and standard high- z galaxy evolution scenarios can be found in Mirocha & Furlanetto (2018). In this paper, we focus on the generic impact of Pop III sources, without direct comparison to the EDGES signal. If the EDGES signal is confirmed by other ground-based experiments (e.g., BIGHORNS,

SCI-HI, SARAS, LEDA; Sokolowski et al. 2015; Voytek et al. 2014; Patra et al. 2015; Bernardi et al. 2016), or space-based experiments (e.g., DARE; Burns et al. 2012, 2017), this paper provides an initial guess for the level of Pop III activity required to explain a 78-MHz absorption trough. If not, the hunt for more subtle signatures of Pop III will resume, following continued improvement in limits at higher frequencies (e.g., Monsalve et al. 2017; Singh et al. 2017).

In Section 2, we will describe our model for Pop II and Pop III stars, and present their global 21-cm signatures in Section 3. We discuss our results in a broader context in Section 4 before concluding in Section 5.

2 MODELS

2.1 Population II star formation

Our model for Pop II star formation is identical to that used in Mirocha et al. (2017), so we only summarize here briefly, and defer the interested reader to that paper for more detail. The underlying model is very similar to others appearing in the literature in recent years (e.g., Mason, Trenti & Treu 2015; Sun & Furlanetto 2016).

Star formation rates in high- z galaxies are assumed to be directly proportional to the growth rates of their dark matter haloes, i.e., $\dot{M}_* \propto f_* \dot{M}_h$. We compute the mass growth rates of haloes by assuming haloes evolve at fixed number density (see, e.g., Furlanetto et al. 2017), which yields results that are broadly consistent with those found in numerical simulations (e.g., McBride, Fakhouri & Ma 2009). We assume the Sheth, Mo & Tormen (2001) form of the halo mass function, which we compute using the HMF code (Murray, Power & Robotham 2013).

We assume that f_* is a double-power law,

$$f_{*,\text{II}}(M_h, z) = \frac{f_{*,0}}{\left(\frac{M_h}{M_p}\right)^{\gamma_{\text{lo}}} + \left(\frac{M_h}{M_p}\right)^{\gamma_{\text{hi}}}} \quad (1)$$

and calibrate its parameters by fitting to the $z \sim 6$ luminosity function measurements from Bouwens et al. (2015). Use of, for example, the measurements of Finkelstein et al. (2015) instead results in a ~ 10 per cent difference in the overall normalization of the SFE, which is not enough to qualitatively change our conclusions. Our default case assumes that this SFE is constant in time.

Finally, we note that our default Pop II model adopts the BPASS version 1.0 single-star models. This results in Lyman–Werner (LW) and Lyman–continuum (LyC) yields of order $\sim 2 \times 10^4$ photons per stellar baryon, much smaller than the yields expected of massive Pop III stars, of order $N_{\text{LW}} \sim N_{\text{ion}} \sim 10^5$ photons per baryon (Schaerer 2002).

2.2 X-rays from Pop II haloes

In addition to the double power-law SFE model, the other critical assumption made in Mirocha et al. (2017) was to adopt the empirical relation between X-ray luminosity and SFR (L_X -SFR) as found in Mineo, Gilfanov & Sunyaev (2012), with a metallicity-dependence motivated by recent theoretical (Fragos et al. 2013) and observational (Brorby et al. 2016) findings.

In the next section, we will assume that Pop III X-ray emission analogously tracks the Pop III SFR, but because there is no empirically calibrated relation, it will be useful to have a simple model to guide us. Readers already familiar with the physical arguments used to explain the L_X -SFR relation may skip ahead to Section 2.3.

As in, e.g., Mirabel et al. (2011), we estimate the X-ray emission from high-mass X-ray binaries (HMXBs) simply as the product of the number of systems in each galaxy, N_{HMXB} , and the typical luminosity of each system, \mathcal{L}_\bullet , i.e.,

$$L_X = N_{\text{HMXB}} \mathcal{L}_\bullet. \quad (2)$$

We assume Eddington-limited accretion with efficiency ϵ , which sets the typical luminosity,

$$\mathcal{L}_\bullet = 1.26 \times 10^{38} \text{ erg s}^{-1} \left(\frac{M_\bullet}{10 M_\odot} \right) \left(\frac{\epsilon}{0.1} \right) \left(\frac{f_{0.5-8}}{0.84} \right), \quad (3)$$

where the factor $f_{0.5-8} = 0.84$ above is the fraction of energy emitted in the 0.5–8 keV band for a $10 M_\odot$ black hole (BH) with a multicolour disk (MCD) spectrum (Mitsuda et al. 1984). For an MCD spectrum, we find that the dependence of $f_{0.5-8 \text{ keV}} = 0.84$ on BH mass is well approximated (over $10 \leq M_\bullet/M_\odot \leq 10^6$) by $f_{0.5-8 \text{ keV}} \sim \exp[-(M_\bullet/1574)^{0.34}]$, so even an order of magnitude change in the characteristic mass of remnants has only a mild impact on L_X^1 .

In some cases, spectral hardening can be an important consideration, even if the 0.5–8 keV luminosity remains fixed. For example, hardening via attenuation by neutral gas can affect the global 21-cm signal at the ~ 50 mK level (for column densities of $N_{\text{H I}} \sim 10^{22} \text{ cm}^{-2}$), whereas hardening due to the upscattering of disk photons by a hot corona (e.g., as in the SIMPL model; Steiner et al. 2009) is only a minor ~ 10 – 20 mK effect (Mirocha 2014). We neglect such complications² because, though they may bias inferred L_X/SFR values, they are unlikely to change the shape of the 21-cm signal, since the X-ray emission still traces the (continually rising) star formation.

Moving on, we can estimate the number of HMXB systems in a galaxy by assuming a constant SFR, and further assuming that some fraction f_\bullet of the mass ends up in neutron stars or black holes, of which a fraction f_{bin} form in binaries, and only a fraction f_{sur} binaries survive the first supernova. Furthermore, we assume that each system is active for some fraction f_{act} of its lifetime, τ , which yields

$$N_{\text{HMXB}} = 20 \left(\frac{\dot{M}_*}{M_\odot \text{ yr}^{-1}} \right) \left(\frac{f_\bullet}{10^{-3}} \right) \left(\frac{M_\bullet}{10 M_\odot} \right)^{-1} \times \left(\frac{f_{\text{bin}}}{0.5} \right) \left(\frac{\tau}{20 \text{ Myr}} \right) \left(\frac{f_{\text{sur}}}{0.2} \right) \left(\frac{f_{\text{act}}}{0.1} \right). \quad (4)$$

Here, $f_\bullet = 10^{-3}$ is the fraction of mass which forms stars with $M_* > 8 M_\odot$ assuming a Chabrier IMF. The corresponding figures for Salpeter and Kroupa IMFs are $f_\bullet = 2 \times 10^{-3}$ and 6×10^{-3} , respectively. Many of the other factors seem reasonable, but strong arguments beyond the factor of \sim few level are lacking. The combination we have chosen is largely with hindsight, knowing that the canonical normalization of the 0.5–8 keV L_X –SFR relation is $c_X \sim 2.6 \times 10^{39} \text{ erg s}^{-1} (M_\odot/\text{yr})^{-1}$, which the product of equations (3) and (4) roughly yield.

This is a very simple argument, resulting in an equation with many highly uncertain factors. In reality, for example, there is a distribution of luminosities among HMXBs. Though the slope of this

distribution function can be explained by fairly simple arguments (Postnov 2003; Mineo et al. 2012), there are still many complex aspects of the HMXB population that we have completely neglected. For example, we have effectively assumed that all systems (when ‘on’) reside in the high-soft state (HSS) given our choice of MCD spectrum with no high-energy tail, though, of course, many known systems are in the low-hard state. The relative amount of time spent in each – and why systems transition from one state to the other – are active areas of research (for a recent review, see, e.g., Belloni 2010), and we have made no attempt to model these factors. This choice, of pure MCD over an SIMPL spectrum, has little effect on the thermal history (Mirocha 2014), but may be an important distinction if concerned with the $z = 0$ unresolved X-ray background (see Section 3.3).

Nonetheless, because the preceding arguments seem to work reasonably well, we employ them again for Pop III star formation in Section 2.4. The key point is that if the Pop III IMF is very top-heavy, $f_\bullet \gg 10^{-3}$, the Pop III L_X/SFR ratio may be larger than that of Pop II sources by up to a factor of $\sim 10^3$.

2.3 Population III star formation

Even upon changes to the stellar metallicity, Z , normalization and Z -dependence of the L_X –SFR relation, neutral gas contents of galaxies, and evolution of the SFE, Mirocha et al. (2017) found that a deep ($\delta T_b \lesssim -150$ mK) and late ($\nu \gtrsim 100$ MHz) absorption feature in the global 21-cm signal persisted. This is due to the decline in the SFE in low-mass haloes (implied by the LF faint-end slope), which causes the SFRD to also be a steep function of redshift, confining the bulk of UV and X-ray photon production to relatively late times ($z \lesssim 12$). The only exception is if there is a floor in the SFE (steepening in LF faint-end slope), especially if $T_{\text{min}} \ll 10^4$ K, which can drive the absorption trough to lower frequencies.

However, in Mirocha et al. (2017), we assumed that the $T_{\text{vir}} < 10^4$ K haloes either shared the same properties as the atomic-cooling haloes, or did not host star formation at all, both of which are unlikely to be true. Our new models treat these low-mass potentially Pop III-hosting haloes in a simple but physically motivated way that allows their properties to differ from their more massive descendants.

A minimally descriptive model of Pop III star formation must explicitly model (or make assumptions about):

- (i) The minimum mass of Pop III star-forming haloes, M_{min} .
- (ii) The star formation history in individual haloes during their Pop III phase.
- (iii) The Pop III stellar initial mass function and atmospheric properties.
- (iv) The condition which, if met, results in a transition from Pop III to Pop II star formation.

All items in this list are coupled, since the minimum mass of Pop III star-forming haloes is set by the strength of the LW background (Haiman, Rees & Loeb 1997), which depends on the population-integrated LW emissivity of Pop III haloes, which depends on M_{min} and the SFHs of Pop III haloes, and so on.

In the following subsections, we describe these four components in more detail.

2.3.1 The minimum mass

We begin all calculations at $z_i = 60$, and take $M_{\text{min, vir}}$ to be the mass corresponding to haloes with virial temperatures of 500 K (Tegmark

¹Note that our expression is slightly different from that in Mirabel et al. (2011), as we consider MCD spectra in the 0.5–8 keV band rather than power-law spectra in the 2–10 keV band.

²It could also be that the MCD and SIMPL models are simply not representative of real sources at photon energies $h\nu \lesssim 1$ keV, for which observational constraints are poor.

et al. 1997). This mass, set by H_2 cooling arguments in the absence of an LW background, exceeds both the Jeans mass and filtering mass at high- z (Naoz & Barkana 2007). Once the first sources form, $M_{\min, \text{III}}$ quickly rises in response to the growing LW background, rendering our results insensitive to the exact choice of the initial critical mass threshold. The supersonic velocity offset between dark matter and baryons after recombination (Tselikhovich & Hirata 2010) can modify this initial mass, and thus, in principle, delay the onset of first-star formation and affect the 21-cm background (Fialkov et al. 2012; McQuinn & O’Leary 2012) will neglect this effect in this work, as it seems to be relatively minor, at least for the global 21-cm signal (Fialkov et al. 2014).

Once Pop III stars begin forming, they generate a diffuse LW background (with mean intensity J_{LW}) that can, in principle, globally regulate star formation by raising the minimum mass threshold (Haiman et al. 1997). To include this effect, we assume the $M_{\min}(J_{\text{LW}})$ relation of Visbal et al. (2014) (their equation 4), and solve iteratively for $M_{\min, \text{III}}$ and J_{LW} , requiring that the Pop III SFRD has converged to a relative accuracy of better than 5 per cent at all redshifts before computing the global 21-cm signal. Typically, only ~ 5 – 10 iterations are required in order to reach convergence³. An example $M_{\min}(z)$ curve is shown in green in Fig. 1, along with relationships between halo age and binding energy, to be discussed further in Section 2.3.4.

But first, because the detailed properties of Pop III stars govern the strength of the diffuse LW background and thus M_{\min} , we focus on them next in Section 2.3.2.

2.3.2 Pop III star formation histories

We assume that each Pop III star-forming halo has a single star-forming region (e.g., O’Shea & Norman 2007). We assume also that each episode of star formation produces the same mass in Pop III stars, on average, which will write as the product of the typical number of stars and their characteristic mass, $N_{*, \text{III}} M_{*, \text{III}}$, to build intuition in what follows. Given a typical lifetime of τ_{III} and a ‘recovery time’ between star-forming episodes⁴, τ_{recov} , the mean SFR in Pop III haloes can be written as

$$\dot{M}_{*, \text{III}} = \frac{N_{*, \text{III}} M_{*, \text{III}}}{\tau_{\text{III}} + \tau_{\text{recov}}}. \quad (5)$$

If Pop III stars are massive ($M_{*, \text{III}} \sim 100 M_{\odot}$) and form in isolation ($N_{*, \text{III}} = 1$), with a typical lifetime of order $\tau_{\text{III}} \sim 5$ Myr and no recovery time (i.e., they form one after the next), then $\dot{M}_{*, \text{III}} = 2 \times 10^{-5} M_{\odot} \text{ yr}^{-1}$. Compared to Pop II haloes, in which $\dot{M}_{*, \text{II}} \propto M_h^{5/3} (1+z)^{5/2}$ (roughly), Pop III haloes form stars much less efficiently. For example, if we define a Pop III SFE that is analogous to the Pop II SFE (i.e., relative to halo growth rate) for

³Scenarios with very efficient Pop III star formation can drive rapid evolution in M_{\min} , which can lead to the need for many iterations (\sim dozens) to reach convergence. To reduce computational time, we have found that simply averaging subsequent solutions for M_{\min} every ~ 5 iterations damps out sharp features that arise in M_{\min} solutions under these circumstances.

⁴Note that numerical simulations suggest that the recovery time could be as short as 10–20 Myr (e.g., O’Shea et al. 2005), or as long as a Hubble time, depending on Pop III stellar mass (Jeon et al. 2014), which would drive $\dot{M}_{*, \text{III}}$ to values lower than $\sim 10^{-5} M_{\odot} \text{ yr}^{-1}$. However Pop III stars may also form in larger numbers with a spectrum of masses (e.g., Hirano et al. 2014). So the $\dot{M}_{*, \text{III}} \sim 2 \times 10^{-5} M_{\odot} \text{ yr}^{-1}$ quoted here should only be considered a rough estimate.

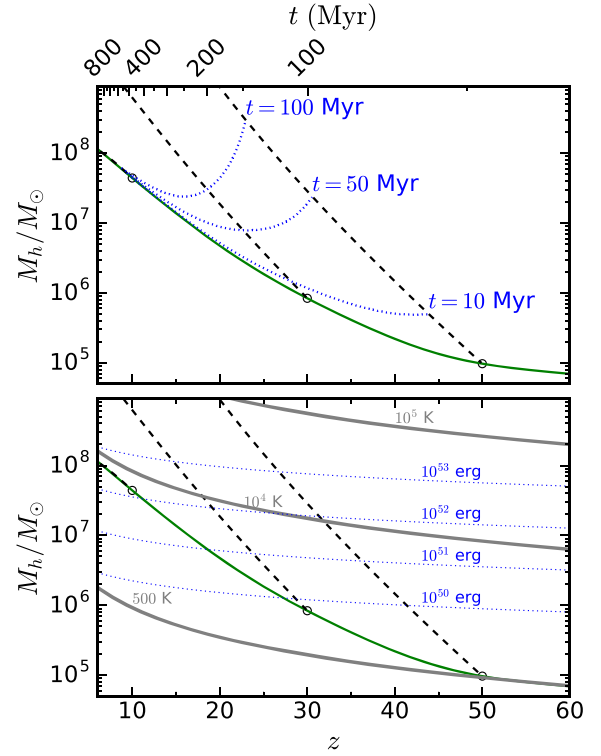


Figure 1. Relationships between halo mass, age, and binding energy as a function of redshift. *Bottom:* Lines of constant virial temperature (grey), binding energy (dotted blue), an example minimum mass curve (green), along with the growth histories of haloes forming at $z = 10, 20$, and 30 (dashed black). *Top:* Lines of constant halo age (dashed blue), as well as the same halo growth histories that are shown in the bottom panel. Note that in both panels, dotted blue lines highlight the means by which we trigger the transition from Pop III to Pop II star formation.

a rough comparison, then $\dot{f}_{*, \text{III}} \sim M_h^{-1} (1+z)^{-5/2}$. This scaling ignores the potential connection between, for example, the recovery time and mass accretion rates, but serves to illustrate the qualitative difference between the efficiency of Pop II and Pop III star formation in our model. In practice, we do not choose each quantity in equation (5) separately, but instead treat $\dot{M}_{*, \text{III}}$ itself as our main free parameter⁵.

The assumption of a single site of star formation results in a Pop III SFRD that is proportional to the number of Pop III haloes between the minimum mass, M_{\min} , and some maximum mass, M_{\max} , that is determined by our transition criteria, i.e.,

$$\dot{\rho}_{*, \text{III}} = \dot{M}_{*, \text{III}} \int_{M_{\min, \text{III}}}^{M_{\max, \text{III}}} \frac{dn}{dm} dm. \quad (6)$$

Here, dn/dm is the mass function of dark matter haloes. We assume that Pop II star formation commences immediately after the Pop III epoch, i.e., $M_{\min, \text{II}} \equiv M_{\max, \text{III}}$. We set $M_{\max, \text{III}}$ via simple arguments outlined in the next subsection, and shown graphically in Fig. 1.

In most of our models, the total number density of Pop III star-forming haloes is $\sim 1 - 10 \text{ cMpc}^{-3}$ at the peak of Pop III star formation, which is why the Pop III SFRD generally peaks at values

⁵For individual haloes this SFR is ill-defined, since the ‘true’ history is a series of discrete bursts. It should be treated as a population-averaged quantity.

of order $\sim \dot{M}_{*,\text{III}} \text{ cMpc}^{-3}$ (as shown in Fig. 2), which we will see in detail in the next section.

2.3.3 Properties of Pop III stars

For the bulk of this study, we assume that Pop III stars are massive, $\sim 100 M_{\odot}$ stars. Though more recent work has highlighted the possibility of a broad Pop III mass spectrum (Turk, Abel & O’Shea 2009; Hosokawa et al. 2011; Hirano et al. 2014), we focus on the solitary massive-star hypothesis as an extreme test case in which Pop II and Pop III stars are wildly different.

We derive UV photon yields for Pop III stars from Schaerer (2002) (the time-averaged properties in his Table 4). Our reference model assumes $120 M_{\odot}$ stars, which emit 1.4×10^{50} Hydrogen-ionizing photons per second, and 1.6×10^{50} LW photons per second averaged over their 2.5 Myr lifetime. For stars more massive than $60 M_{\odot}$, lifetime-integrated yields change by only ~ 10 per cent, since the lower mass stars are less luminous but also live longer. It is these lifetime-integrated values for LyC and LW photon production, commonly denoted with N_{ion} and N_{LW} , respectively, that we use to convert star formation rates to LyC and LW photon production rates throughout.

Note that our parametrization does not necessarily exclude the possibility of lower mass Pop III stars, since the radiative yield (a function of stellar mass) is degenerate with the efficiency of Pop III star formation. We will explore the effects of stellar mass and SFE in Section 3.1.

2.3.4 Transition to Pop II star formation

We assume that Pop III stars continue to form at rate $\dot{M}_{*,\text{III}}$ until some set of criteria are met that trigger the transition from Pop III to Pop II star formation. In numerical simulations, a critical metallicity ($Z_c \sim 10^{-3.5}$ Bromm & Loeb 2003), determines whether a cell forms Pop II or Pop III stars. However, because our calculations have no spatial information, we cannot impose the transition based on local gas conditions (we only have global halo properties at our disposal). Mebane et al. (2017) find that use of the *mean* halo metallicity, in lieu of any local metallicity information, can result in Pop III SFHs that resemble those of more sophisticated calculations. We adopt a simpler approach in this work.

We introduce two parameters that aim to bound cases in which the transition to Pop III is triggered either (i) once haloes have generated a sufficient metal mass, and/or (ii) are sufficiently massive that metals produced in supernovae remain gravitationally bound to the halo. The first case is obtained by assuming haloes form Pop III stars for a given amount of time, \mathcal{T}_c , which in our framework is equivalent to assuming that the Pop III phase always results in the same mass in stars or metals (since we assume a constant Pop III SFR in individual haloes). The second limit is obtained by assuming Pop III haloes transition to Pop II star formation once their binding energy exceeds some critical value, \mathcal{E}_c .

Large values of \mathcal{E}_c represent cases in which the supernovae of the first stars are so energetic that material in haloes with $\mathcal{E} < \mathcal{E}_c$ would become completely unbound. Smaller values of \mathcal{E}_c represent cases of less energetic supernovae, which even relatively small haloes can sustain. In reality, there is likely a link between \mathcal{T}_c , \mathcal{E}_c , and $M_{*,\text{III}}$, since presumably the most massive stars produce the most energetic supernovae, and the most energetic supernovae produce the most metals. For example, even haloes that harbor PISN may have comparable Pop III SFHs to haloes that do not, since efficient

metal production may be counteracted by efficient metal expulsion. We make no attempt to model these connections in detail, though such cases do lie within our model grid (see Section 3.2.2). As a result, our model is likely conservative, i.e., it generates a more diverse set of Pop III SFHs than would arise in a more detailed physical model.

Model halo mass growth histories are shown in Fig. 1 for haloes that cross the minimum mass threshold at different times, with lines of constant halo virial temperature, binding energy, and age indicated for reference. The minimum mass curve in this figure is set assuming $\mathcal{T}_c = 2.5$ Myr, $\mathcal{E}_c = 10^{51}$ erg, and $\dot{M}_{*,\text{III}} = 10^{-5} M_{\odot} \text{ yr}^{-1}$. Note that the trajectory of a halo forming at $z \sim 10$ in this model is roughly parallel to the minimum mass curve (due to the decline in halo accretion rates), meaning there will be no new Pop III haloes at $z \lesssim 10$.

When operating in isolation, each transition mechanism produces qualitatively similar Pop III SFRDs, as shown in the left and centre columns of Fig. 2. Both lead to rising SFRDs at early times, which eventually peak (or plateau) before tending to zero at late times (in most cases). The most noticeable difference between the \mathcal{T}_c -limited (left) and \mathcal{E}_c -limited (middle) models is that the latter can produce very sharp Pop III SFRDs which rise and fall rapidly at early times. Note that similar histories can also occur if M_{min} rises above the atomic-cooling threshold at early times (if, e.g., Pop II star formation is very efficient and generates a strong LW background; Mebane et al. 2017), enabling the formation of metal-free stellar populations with a normal IMF. Such stars are still technically Pop III, though for our purposes, and in Mebane et al. (2017), it is appropriate to count such haloes in the Pop II SFRD since it is the most massive stars (and their remnants) to which the global 21-cm signal and PISN rates are most sensitive. We will revisit this point in Section 3.1, as such histories have a particularly distinct impact on the global 21-cm signal.

If \mathcal{T}_c and \mathcal{E}_c are both non-zero, they can combine to produce multi-component SFRDs, the features of which are often sharp given the simplicity of our model (right column of Fig. 2). Though likely unrealistic, we make no effort to smooth out such features as they make it easy to visually identify when the Pop III SFRD is governed by \mathcal{T}_c or \mathcal{E}_c , both in the SFRD itself, as well as the global 21-cm signal (see Section 3). If the values are just right, the SFRDs can be smooth, and sometimes very nearly flat.

These results are subject to the assumed production efficiency of LW photons, N_{LW} , which our default ‘massive Pop III’ case assumes is $N_{\text{LW}} \sim 10^5$, as is expected to be the case for $\sim 100 M_{\odot}$ metal-free stars Schaerer (2002). The middle and bottom rows of Fig. 2 change N_{LW} and thus the strength of LW feedback. If LW emission from Pop III stars is reduced, by assuming their properties are comparable to metal-poor stars with a Salpeter IMF (‘normal IMF’), Pop III stars can form in lower mass haloes, and boost the overall SFRD. In the extreme limit of no Pop III LW emission, Pop III star formation is regulated by the Pop II-generated LW background, and can result in strong, very flat Pop III SFHs.

This differences between \mathcal{T}_c and \mathcal{E}_c models can be better understood by referring back to Fig. 1. For \mathcal{T}_c -limited models, the M_{min} and M_{max} curves are quasi-parallel, since the mass range depends on the growth history of haloes (i.e., $M_{\text{min,III}}$ at z sets $M_{\text{max,III}}$ at $z' < z$). The same is not true of the \mathcal{E}_c -limited models, whose $M_{\text{max,III}}$ contours can be drawn without reference to the growth of individual haloes. As a result, the interface between $M_{\text{min,III}}$ and $M_{\text{max,III}}$ can be sharp (the binding energy is only linear in redshift, while M_{min} is typically steeper), and Pop III SFRDs can rapidly decline to zero as $M_{\text{min,III}}$ overtakes $M_{\text{max,III}}$. In other words, there comes a point for

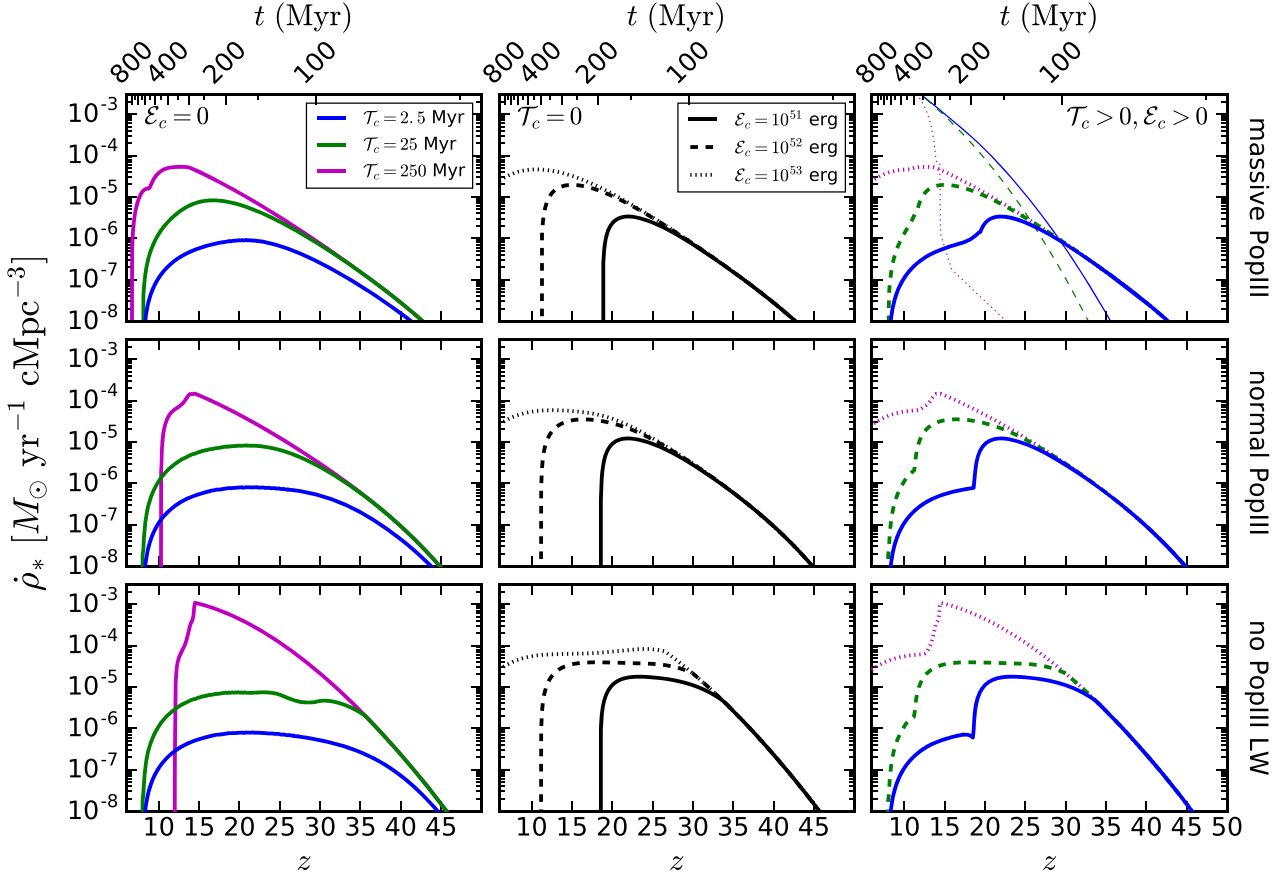


Figure 2. Models for the Pop III star formation rate density, assuming a constant $\dot{M}_{*,\text{III}} = 10^{-5} M_\odot \text{ yr}^{-1}$ in all Pop III haloes. From left to right, we explore the different transition mechanisms, starting with time-limited Pop III star formation (left), binding-energy-limited (middle), and a model in which the both mechanisms are at work (right). Each row adopts a different model for the Pop III stellar properties, from the massive ($120 M_\odot$) case, which sets $N_{\text{LW}} \sim 10^5$ (top), to no LW emission at all (bottom). Example Pop II star formation histories are shown in thin lines in the upper right-hand panel. Note that the inferred SFRD at $z \sim 6$ is of order $\sim \text{few} \times 10^{-2} M_\odot \text{ yr}^{-1} \text{ cMpc}^{-3}$.

\mathcal{E}_c -limited models in which *all* haloes suddenly satisfy the transition criterion, $\mathcal{E} \geq \mathcal{E}_c$, which means they immediately commence Pop II star formation, even if they have yet to form Pop III stars. Note that in this case, if the critical \mathcal{E}_c curve is comparable to the atomic cooling threshold, the stars formed could follow a normal IMF despite still being metal free.

In the $\mathcal{E}_c = 0$ limit, such sharp SFRDs never occur. Pop III star formation will continue globally at some non-zero level until the minimum mass is growing more rapidly than a halo of the minimum mass. In other words, some haloes will be growing too slowly to ever ‘catch up’ with $M_{\text{min,III}}$ and will never be able to form stars at all. In our models, this typically occurs at $z \lesssim 10$ (see Fig. 1, in which a halo forming at $z = 10$ grows at the same rate as $M_{\text{min,III}}$). As in Mebane et al. (2017), this is what ultimately drives Pop III stars to extinction in most models.

2.4 X-rays from Pop III haloes

We also assume that haloes hosting Pop III stars emit X-rays. In general, the emission could come from inverse Compton scattering in supernova remnants, or from bremsstrahlung as ISM gas cools. As our reference case, we assume that some fraction of Pop III stars will form in binaries, and ultimately produce an X-ray binary system, which renders our Pop III model completely analogous to

the Pop II model (see Section 2.2), except for its susceptibility to global LW feedback, and finite lifetime imposed by τ_c and \mathcal{E}_c .

As a result, for Pop III haloes we introduce a scaling factor for the Pop III L_X -SFR relation, $f_{X,\text{III}}$, defined relative to the canonical Pop II L_X -SFR relation, i.e.,

$$L_{X,\text{III}} = f_{X,\text{III}} \times 2.6 \times 10^{39} \text{ erg s}^{-1} (M_\odot/\text{yr})^{-1}. \quad (7)$$

Whereas the local (Pop II) L_X -SFR relation, probably does not grow by more than a factor of ~ 10 as metallicity decreases, equations (3) and (4) tell us that Pop III sources may be $\sim 10^3$ times more efficient at producing X-rays per unit stellar mass formed, if indeed their IMF is top-heavy (i.e., $f_\bullet \gg 10^{-3}$).

Though the typical remnant mass may be larger for Pop III HMXBs, and thus reduce the value of $f_{0.5-8}$ and perhaps also τ , these are likely fairly modest, factor of $\sim \text{few}$, effects. As a result, it is not difficult to imagine a scenario in which Pop III sources are substantially more efficient at producing X-rays than Pop II haloes, so long as f_\bullet is large. If indeed $f_{X,\text{III}} > 1$, the X-ray background will remain dominated by Pop III even after the total SFRD becomes dominated by Pop II sources, the latter of which typically occurs at $15 \lesssim z \lesssim 30$ (see upper right corner of Fig. 2).

Note that we will not explicitly model the binary fraction or Pop III IMF, since $f_{X,\text{III}}$ is also degenerate with $\dot{M}_{*,\text{III}}$. We will thus attempt to qualify expectations for constraining $f_{X,\text{III}}$ and $\dot{M}_{*,\text{III}}$ accordingly throughout.

For the rest of this paper, we assume that the minimum mass is set only by J_{LW} , though in principle M_{min} could depend on the X-ray background as well, since X-rays can boost the electron fraction and thus catalyse H_2 formation in dense clouds (e.g., Machacek, Bryan & Abel 2003; Glover 2016; Ricotti 2016). We will revisit this potential complication in Section 4.

2.5 Generating the Global 21-cm signal

All calculations were conducted with the *ARES* code⁶. *ARES* treats the IGM as a two-phase medium, tracking separately the growth in the volume filling factor of ionized gas and the mean temperature and ionization state of gas in the ‘bulk’ IGM beyond. That is, *ARES* does *not* generate a three-dimensional realization of the 21-cm field using, e.g., seminumeric techniques (Mesinger, Furlanetto & Cen 2011). For a more detailed description of how *ARES* solves for the ionization and thermal histories, see Section 2 of Mirocha (2014).

ARES outsources a few important calculations to well-established software packages. For example, we generate initial conditions for the state of the high- z IGM using the *COSMOREC* code (Chluba & Thomas 2011), and halo mass functions using the *HMF-CALC* code (Murray et al. 2013), which itself depends on the *Code for Anisotropies in the Microwave Background* (CAMB; Lewis, Challinor & Lasenby 2000).

A few additional notes are warranted regarding various atomic physics calculations that occur within *ARES*.

We compute the rate of collisional excitation/de-excitation of the hyperfine states using the tabulated values in Zygelman (2005) and take the radiative coupling coefficient (Wouthuysen 1952; Field 1958) to be $x_\alpha = 1.81 \times 10^{11} \hat{J}_\alpha S_\alpha / (1 + z)$, where S_α is a factor of order unity that accounts for line profile effects (Chen & Miralda-Escudé 2004; Furlanetto & Pritchard 2006; Chuzhoy, Alvarez & Shapiro 2006; Hirata 2006), and \hat{J}_α is the intensity of the Ly- α background in units of $\text{s}^{-1} \text{cm}^{-2} \text{Hz}^{-1} \text{sr}^{-1}$. We adopt the formulae from Furlanetto & Pritchard (2006) to compute S_α .

In addition, we follow Pritchard & Furlanetto (2006) in computing the fraction of Ly- n photons that cascade through the Ly- α resonance, and use the lookup tables of Furlanetto & Johnson Storer (2010) to determine the fraction of energy that photoelectrons deposit as heat, further ionization, and excitation in the gas⁷. We use the fits of Verner & Ferland (1996) for bound-free absorption cross-sections, and adopt the formulae for recombination and cooling rate coefficients from the appendices of Fukugita & Kawasaki (1994).

We adopt *Planck* cosmological parameters (Planck Collaboration et al. 2016a) throughout.

3 RESULTS

In this section, we focus on how Pop III stars affect the global 21-cm signal. First, we explore a small set of realizations to build some intuition (Section 3.1). Then, we move on to an expanded grid of models, and attempt to determine if the Pop III-induced modulations of the signal are generically distinct from those brought about by variations in the parameters governing Pop II star formation (Section 3.2.2). To close the section, we examine whether any of

our Pop III scenarios are in tension with pre-existing measurements (Section 3.3).

3.1 Pop III Signatures: Basic Features

In Fig. 3, we show several realizations of the global 21-cm signal assuming different models for Pop III stars, but holding the Pop II component of the model fixed. In each row, we assume a different Pop III SFR per halo, $\dot{M}_{*,\text{III}}$, while each column adopts a different transition mechanism, including time (left), binding energy (middle), and a scenario in which both of these mechanisms are at work, and correlated with each other (right). The width of each semi-transparent band corresponds to a factor of 2 change in $f_{X,\text{III}}$, from $25 \leq f_{X,\text{III}} \leq 3200$. The lower limit of 25 was chosen because it is usually the point when the trough depth first comes to be visibly affected by Pop III sources. The upper limit of 3200 does not correspond directly to a special case, though is about the limit of what one would expect for a source population of exclusively $100 M_\odot$ stars that all form in binaries (see equations (3)–(4)). For reference, the most opaque band corresponds to $200 \leq f_{X,\text{III}} \leq 400$.

Each panel also shows three example Pop II-only models with increasingly efficient X-ray heating. The model with the deepest trough is our reference Pop II-only model (referred to as the *dp1* model in Mirocha et al. 2017), while the intermediate case assumes low metallicity star-forming regions and a strong connection between L_X -SFR and Z (as $L_X \propto Z^{-0.6}$), which boost L_X/SFR by a factor of 9. Unless there are much more efficient X-ray sources at high- z , these realizations roughly span the range of expected trough depths. The model with the weakest trough adds a new population of X-ray sources with a soft (unabsorbed) $\alpha_X = -1.5$ power-law spectrum that produces 0.5–8 keV photons 10 times more efficiently than our default model, i.e., with $L_X/\text{SFR} = 2.6 \times 10^{40} \text{ erg s}^{-1} (M_\odot/\text{yr})^{-1}$.

The top row of Fig. 3 is most similar to the ‘classic’ conception of Pop III as isolated, massive, short-lived stars, since $\dot{M}_{*,\text{III}} \sim 10^{-5}$ corresponds to a single $100 M_\odot$ star forming every 10 Myr (via equation (5)). In this case, the frequency of the absorption minimum is hardly affected, though its amplitude can be reduced if $f_{X,\text{III}} \gg 1$. If the binding energy is an important factor in the transition to Pop II star formation (centre and right columns), the low-frequency tail of the absorption trough grows slightly, as Pop III star formation is effectively allowed to persist for longer times in very high- z haloes.

At this stage, the *absolute* depth of the absorption trough appears not to be a powerful discriminant between Pop II+Pop III models (green) and Pop II-only models (grey), as considerable uncertainty (to be explored further in the next section) in Pop II sources still remains. However, the depth of the trough *relative* to the emission peak, and the timing between extrema of the signal, appear to have more potential. For example, even as the trough becomes shallower in Pop III models, the emission maximum remains largely unchanged. Such behaviour is not seen in Pop II-only models, in which reductions in the trough amplitude give rise to stronger emission features. This is because heating of the IGM is driven by sources whose SFRD rises monotonically with time, whereas Pop III sources provide ‘extra’ heating only at early times. This decoupling of the amplitudes of the minimum and maximum leads to very broad, asymmetric absorption signals.

This general trend continues as we increase $\dot{M}_{*,\text{III}}$ in the middle and bottom rows of Fig. 3. In extreme cases, a second absorption trough appears (centre column, bottom two rows). Such behaviour is probably unlikely, as it requires strong ($\dot{M}_{*,\text{III}} \gtrsim 10^{-4} M_\odot \text{ yr}^{-1}$) but globally short-lived ($\tau \gtrsim 20$ only) Pop III star formation, so that the UV background generated by Pop II sources is not strong

⁶<https://bitbucket.org/mirochaj/ares; v0.4>

⁷While photo-electrons can excite Ly- α and thus in principle allow the X-ray background to contribute to Wouthuysen-Field coupling, we find this effect to be negligible unless $f_{X,\text{III}} \gtrsim 10^3$.

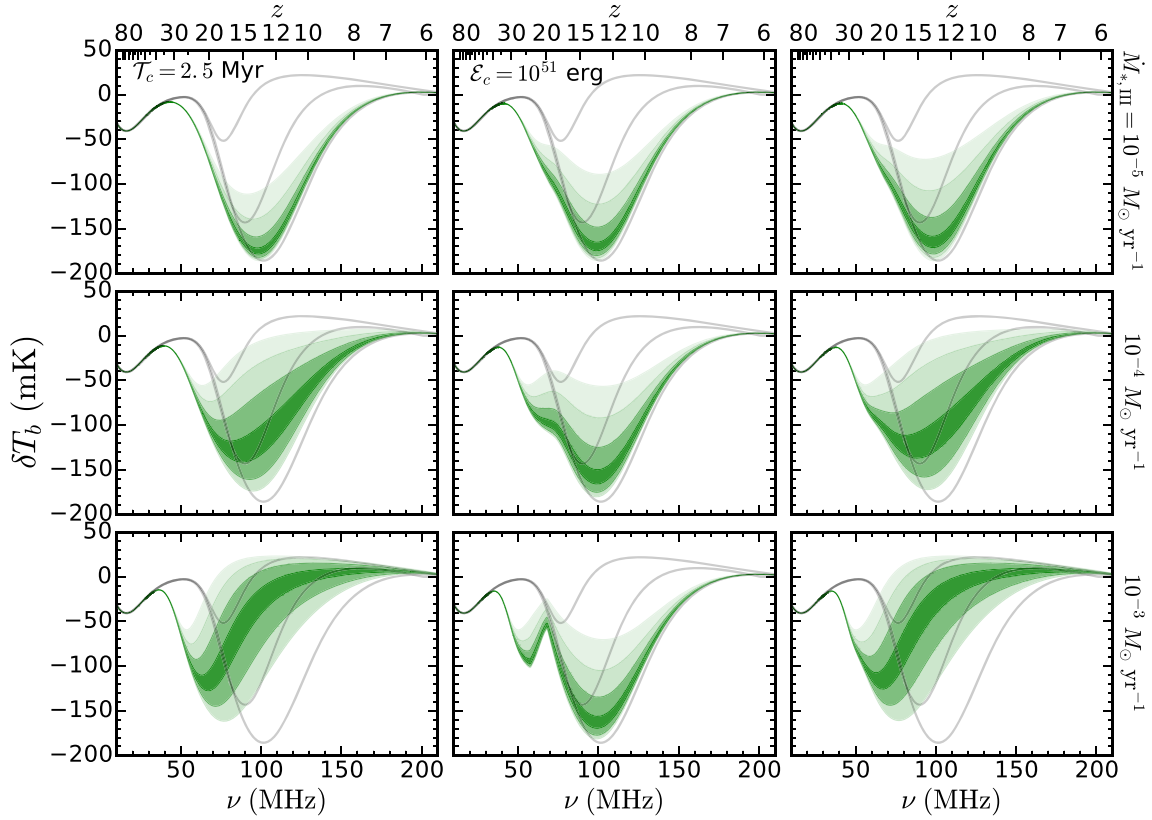


Figure 3. Global 21-cm signal realizations with Pop III sources. From top to bottom, each row assumes increasingly efficient Pop III star formation in individual haloes, while each column explores a different transition mechanism, including pure time-limited cases ($\mathcal{T}_c = 2.5$ Myr; left), pure binding-energy-limited cases ($\mathcal{E}_c = 10^{51}$ erg; middle), and a case with both effects in operation (right; colours and line-styles correspond to first two columns). The width of each coloured band corresponds to a factor of 32 change in $f_{X,III}$ over the interval ($25 \leq f_{X,III} \leq 3200$), with individual factor of 2 changes indicated by opacity. For example, the most opaque band corresponds to $200 \leq f_{X,III} \leq 400$. Three example Pop II-only realizations are shown in grey in each panel, each with increasingly efficient heating, which drive both weaker troughs and stronger emission features.

enough to maintain the Wouthuysen-Field coupling after Pop III stars die out. In our model, this is only achieved if $\mathcal{T}_c \sim 0$, since haloes can effectively skip the Pop III phase if their binding energy already exceeds \mathcal{E}_c when they cross the minimum mass threshold. Even a single, short-lived episode of Pop III star formation can prevent the emergence of a double trough⁸ (right column, bottom two rows). The binding energy alone is probably not a sufficient criterion for triggering the transition to Pop II star formation, as it does not influence the cooling properties of gas in high- z haloes.⁹

Note that in Fig. 3, as in Fig. 2, we have assumed massive $120 M_\odot$ Pop III stars, so the SFR values explored from top to bottom should really be interpreted as the product $\dot{M}_{*,III}(N_{LW}/10^5)$. This implies that Pop III sources with a more normal IMF (and $N_{LW} \sim 10^4$) will have a less dramatic effect on the 21-cm signal. We will revisit this point in Section 4.2.

⁸Another way for haloes to skip the Pop III phase if metals expelled by neighbouring haloes are accreted before stars form (Smith et al. 2015), though it seems unlikely that such a process could affect enough haloes at early times to completely eliminate Pop III star formation globally given the generally low volume-filling fraction of metals seen in simulations (e.g., Jaacks et al. 2018).

⁹Except if that critical binding energy is $\sim 10^{51.5} - 10^{52}$ erg at $z \gtrsim 30$, which are comparable to the atomic cooling threshold, though with milder redshift evolution. See the bottom panel of Fig. 1.

Given the observational implications of a double trough, the likelihood of a rapid rise and fall in the Pop III SFRD warrants further discussion, which we also defer to Section 4.2.

3.2 Are broad asymmetric troughs a generic feature of Pop III?

In the previous section, we showed a small set of representative Pop III SFRDs and the corresponding global 21-cm spectra for select values of \mathcal{T}_c and \mathcal{E}_c . Our goal in the rest of the paper will be to determine if broad asymmetric troughs are a feature of Pop III models that is (i) distinguishable from Pop II-only models, and (ii) expected for a broader range of Pop III models.

3.2.1 A large set of Pop II-only models

To determine if the presence of Pop III can be detected despite uncertainties in our understanding of Pop II galaxies, we generate a superset of the Mirocha et al. (2017) models ($N = 10^5$ of them) by Monte Carlo sampling the parameter space defined in Table 1 and shown graphically in Fig. 4.

The bounds of this parameter space are chosen to encompass:

- (i) The range of single-star spectral models in BPASS version 1.0 (Eldridge & Stanway 2009) over the entire metallicity range, $0.001 \leq Z \leq 0.04$. Use of the version 1.0 BPASS models is to maintain

Table 1. Parameter space surveyed for Pop II models. Each row provides information for a different free parameter (introduced in text), with the range of values surveyed first for the most conservative set (middle), and then for a more restrictive set as described in the text (right).

Name	Full range	Refined range
Z	[0.001, 0.04]	[0.001, 0.003]
γ_z	[-1, 1]	[-0.1, 0.1]
M_c/M_\odot	$[10^7, 10^{11}]$	$[10^7, 10^9]$
c_X	$[1, 5] \times 10^{39} \text{ erg s}^{-1} (M_\odot/\text{yr})^{-1}$	
β_X	[-0.8, 0]	[-0.7, -0.5]
N_{HI}	$[10^{19}, 10^{22}] \text{ cm}^{-2}$	
$f_{\text{esc}, L\gamma C}$	[0.01, 0.3]	

consistency with the Mirocha et al. (2017) models, but note that β_X (see next bullet) has a larger impact than Z itself, given that we force our models to match the galaxy LF (see Fig. 5 and associated text in Mirocha et al. 2017).

(ii) Uncertainties in the $z = 0$ L_X –SFR relation (factor of 5), and its dependence on metallicity ($L_X \propto Z^{\beta_X}$), from Z -independent all the way up to $\beta_X = -0.8$ (slightly steeper than the preferred value in Brorby et al. 2016).

(iii) Uncertainty in the redshift evolution of the SFE of Pop II haloes, which we allow to evolve as a power-law with index γ_z , between $f_* \propto (1+z)^{-1}$ and $f_* \propto (1+z)^1$. Simple models suggest a mild $(1+z)^{1/2}$ – $(1+z)$ dependence (Furlanetto et al. 2017), but observations at high- z are roughly consistent with all of these scenarios (Sun & Furlanetto 2016; Mirocha et al. 2017).

(iv) Uncertainty in the faint-end slope of the LF, which we model allowing the low-mass SFE to steepen as $f_*(M_h) = \left[1 + (2^{\mu/3} - 1) \left(\frac{M_h}{M_c}\right)^{-\mu}\right]^{-3/\mu}$, as in O’Shea et al. (2015). We take $\mu = 1$ and vary M_c as a free parameter.

(v) Uncertainty in the escape of X-ray photons, as parametrized by a characteristic neutral column density, N_{HI} , in a range consistent with what is seen (at least in low-mass $10^7 - 10^8 M_\odot$ haloes) in simulations (Das et al. 2017). We include the opacity of neutral hydrogen and helium, but neglect contributions from HeII and metals.

The basic properties of this model set are shown in Fig. 4. In the left panel, we show the reference model from Mirocha et al. (2017), in addition to contours bounding the location of the absorption minimum in all models in our MC-generated set (see Table 1). As expected, models are roughly centred on our reference Pop II-only, with $\nu_{\text{min}} \sim 100$ MHz and $\delta T_b(\nu_{\text{min}}) \sim -180$ mK¹⁰. Note that our reference Pop II-only model is similar to other models in the literature, for example the BRIGHT GALAXIES model of Mesinger, Greig & Sobacchi (2016).

Models with deeper troughs at higher frequencies than those in our reference Pop II-only model have harder X-ray spectra, less efficient star formation, and/or less efficient X-ray production per unit SFR (e.g., $\beta_X \sim 0$ or small c_X). Shallower and earlier troughs occur when $Z \ll Z_\odot$, when the L_X –SFR relation depends strongly on Z ($\beta_X \ll 0$), and/or when the intrinsic absorption in host galaxies is minimal. We find that strong neutral absorption (at the level of

$N_{\text{HI}} \sim 10^{21.5} \text{ cm}^{-2}$) almost exactly counteracts the more efficient heating caused by low- Z boosts to the L_X –SFR relation, and results in global 21-cm spectra consistent with the pure Pop II-only model.

Our most conservative bounds on Pop II models are represented by the largest black contour, with a more refined set of models bounded by the inner contour, that assumes that the SFE of Pop II haloes does not evolve with time, that high- z galaxies are low metallicity ($0.001 \leq Z \leq 0.003$), and that low Z is reflected both in the UV spectrum of sources and their X-ray emissions (by limiting $-0.7 \leq \beta_X \leq -0.5$, i.e., assuming the Brorby et al. (2016) best-fit is correct). There are simple theoretical arguments in support of each refinement, though current measurements do not require such revisions to the model. For that reason, the inner contours are meant to indicate how progress in the coming years, e.g., better constraints on the redshift evolution of the LF and metallicities of very high- z galaxies, might feed back into the calibration of our Pop II-only models and thus enhance our sensitivity to Pop III sources.

In the centre panel, we focus on two new metrics of the shape of the signal. First, we introduce a measure of the asymmetry of the signal, \mathcal{A} , which we define as the difference in width of the trough measured at half its maximal amplitude,

$$\mathcal{A} = |\nu^+ - \nu_{\text{min}}| - |\nu^- - \nu_{\text{min}}| \quad (8)$$

where ν^+ and ν^- refer to the frequencies above and below the extremum at half its maximal amplitude, respectively, and ν_{min} is the frequency of the extremum itself. A value of $\mathcal{A} = 0$ indicates a symmetric absorption trough, at least at its half-max point, while positive (negative) values arise when the signal is skewed to higher (lower) frequencies¹¹. Our Pop II-only models tend to be only mildly skewed, with $\mathcal{A} \sim 0 \pm 5$ MHz, and a smaller tail out to $\mathcal{A} \lesssim -10$ MHz. The most negatively skewed realizations occur when Wouthuysen–Field coupling is strong at early times but heating occurs late or not at all.

We also quantify the prominence of the ‘wings’ of the signal as the ratio of the trough’s full-width at half-max¹² (FWHM) to its depth,

$$\mathcal{W} = \frac{\text{FWHM}}{\delta T_b(\nu_{\text{min}})} \quad (9)$$

For Pop II-only models, we find that $\mathcal{W} \sim 0.26 \pm 0.06 \text{ mK MHz}^{-1}$, i.e., they are typically ~ 3 – 5 times deeper than they are wide.

In the right-hand panel of Fig. 4, we also show the mean slope of the signal at frequencies between the first two extrema, $\langle \delta T'_b \rangle_{\text{lo}}$, and at frequencies between the absorption minimum and emission maximum, $\langle \delta T'_b \rangle_{\text{hi}}$. These quantities were also recently studied in the semi-numeric models of Cohen et al. (2017), who found a broader range of possibilities, with $-8 \lesssim \langle \delta T'_b \rangle_{\text{lo}}/\text{mK MHz}^{-1} \lesssim -1$ and $1 \lesssim \langle \delta T'_b \rangle_{\text{hi}}/\text{mK MHz}^{-1} \lesssim 6$, in most cases. For now, we simply note that our Pop II models span a narrower range of values, which seems to indicate the effects of calibrating to high- z LF measurements. We defer a more detailed comparison of our model sets to future work.

¹¹We found \mathcal{A} to be a relatively intuitive measure of asymmetry, though there are almost certainly other useful ways to quantify the asymmetry of the signal. We explored several, including the width asymmetry at different amplitudes, slopes at different amplitudes, and the skewness, and found no compelling reason at this time to prefer one over the other.

¹²We prefer the FWHM to the standard deviation at this time since extraction of the latter is likely to be more model-dependent given its dependence on the entire spectrum.

¹⁰Due to a bug in the calculation of S_α in a previous version of ARES, troughs in these models occur slightly (\sim few MHz) earlier than those in Mirocha et al. (2017).

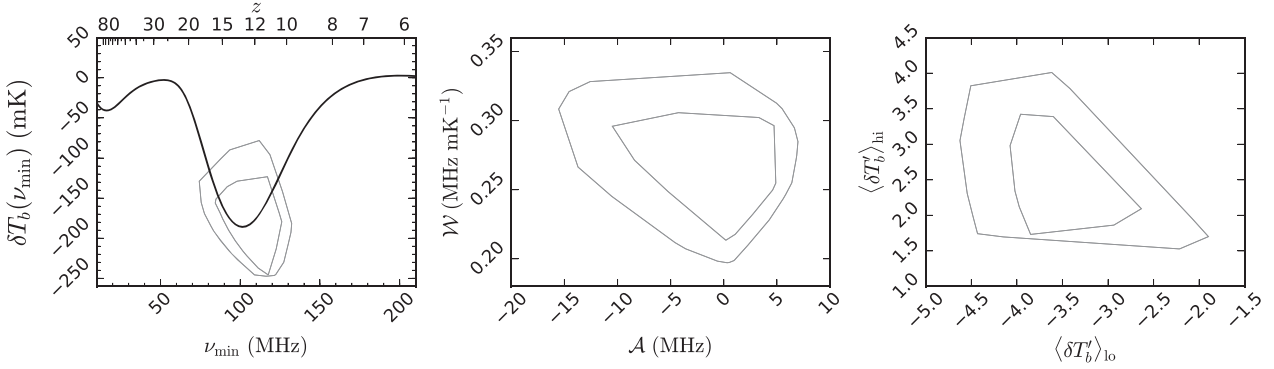


Figure 4. Distillation of the Mirocha et al. (2017) models. *Left:* Fiducial Pop II-only model (solid black curve), with contours enclosing the location of the absorption trough in all realizations (largest polygon), and a refined subset (smaller polygon). *Middle:* Relationship between the asymmetry of the signal, \mathcal{A} (equation (8)), and the prominence of its wings, \mathcal{W} (equation (9)). *Right:* Relationship between the mean slope of the global 21-cm signal, as measured at frequencies between the first extremum and the trough, $\langle \delta T_b' \rangle_{\text{lo}}$, and at frequencies between the absorption trough and emission peak, $\langle \delta T_b' \rangle_{\text{hi}}$.

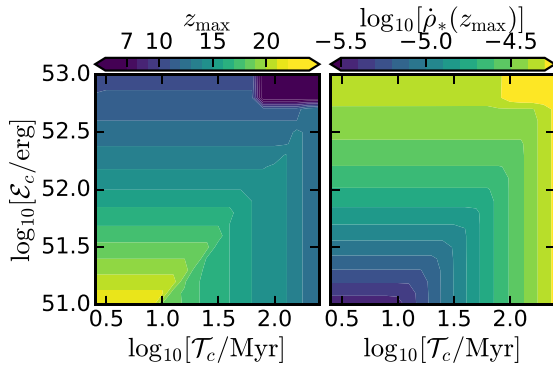


Figure 5. Full set of Pop III SFR models for $\dot{M}_{*,\text{III}} = 10^{-5} M_{\odot} \text{ yr}^{-1}$. Each panel shows a 2-D slice of our Pop III star formation model, \mathcal{T}_c versus \mathcal{E}_c , colour-coded by different metrics of the Pop III SFRD. Pop III SFRDs that peak early ($z_{\text{max}} \gtrsim 20$) reside in the lower-left portion of our parameter space (left panel), while peak Pop III SFRD increases monotonically as \mathcal{T}_c and \mathcal{E}_c grow (right panel).

Table 2. Parameter space surveyed for Pop III models.

Name	Range
$\dot{M}_{*,\text{III}}/M_{\odot} \text{ yr}^{-1}$	$[10^{-6}, 10^{-3}]$
$\mathcal{T}_c / \text{Myr}$	$[2.5, 250]$
$\mathcal{E}_c / \text{erg}$	$[10^{51}, 10^{53}]$
$f_{X,\text{III}}/2.6 \times 10^{39} \text{ erg s}^{-1} (M_{\odot}/\text{yr})^{-1}$	$[0, 3200]$

3.2.2 Expanding the set of Pop III models

To facilitate comparison with the large set of Pop II-only models, we generated a broad set of Pop III models first in a two-dimensional grid over \mathcal{T}_c and \mathcal{E}_c , including values as small as the lifetime of very massive stars ($\mathcal{T}_c \sim 2.5 \text{ Myr}$) and the binding energies of typical supernovae ($\mathcal{E}_c \sim 10^{51} \text{ erg}$), up to a factor of 100 more in each dimension. In subsequent sections, we explore also the effects of $\dot{M}_{*,\text{III}}$ and $f_{X,\text{III}}$, resulting in a final Pop III model grid with four dimensions. A summary of this model grid is included in Table 2

In Fig. 5, we show the bulk properties of the SFRD in this expanded grid of models, including the redshift at which the Pop III SFRD reaches its maximum, z_{max} , and the SFRD at that redshift, $\dot{\rho}_{*,\text{max}}$.

The most salient features of this plot are the anti-correlation between z_{max} and both \mathcal{T}_c and \mathcal{E}_c (left), and the factor of ~ 10 range in peak SFRDs (right). \mathcal{T}_c and \mathcal{E}_c are largely independent, apart from a very mild correlation in the timing of the peak SFRD at small values of each parameter.

3.2.3 Pop II versus Pop III

Now, with large sets of Pop II-only models and models with Pop II and Pop III sources, we can look for distinguishing characteristics of the different model families.

In Fig. 6, we take slices through our set of Pop III models at fixed $f_{X,\text{III}}$ (top) and $\dot{M}_{*,\text{III}}$ (bottom), and compare to the entire set of Pop II-only models (black polygons, identical to those in Fig. 4). For clarity, we do not attempt to colour-code each point in the Pop III parameter space by, e.g., z_{max} or $\dot{\rho}_{*}(z_{\text{max}})$, but simply draw a boundary around the entire set of models in $(\mathcal{T}_c, \mathcal{E}_c)$ space, as we did for the Pop II models. As a result, the shapes in Fig. 6 simply represent the square $(\mathcal{T}_c, \mathcal{E}_c)$ parameter space reprojected into three new planes.

While it is clear that most Pop III models are indistinguishable from Pop II-only models based on the trough's position alone (except if $f_{X,\text{III}} \gtrsim 1600$; upper left panel), there is far less overlap between the Pop II and Pop III models if one focuses on the shape metrics defined by equations (8) and (9) (middle column), or the mean slope of the signal on either side of the trough (right column). This suggests that detailed measurements of the shape of the global 21-cm absorption trough could reveal the presence of Pop III star formation, even if the position of the trough is consistent with Pop II-only models.

For example, consider a scenario in which $f_{X,\text{III}} = 100$. Based on even a precise measurement of the trough, we would be unable to discern the presence of Pop III sources, as the third smallest green polygon sits entirely within the polygon representing even the refined set of Pop II-only models. However, in $(\mathcal{A}, \mathcal{W})$ space (middle panel of Fig. 6), a measurement of $\mathcal{W} \gtrsim 0.3 \text{ mK MHz}^{-1}$ and $\mathcal{A} \gtrsim 7 \text{ MHz}$ would be strong evidence for Pop III.

Unfortunately, moving beyond a simple null test to constrain the parameters of our Pop III model will be very difficult. This is, in part, due to uncertainties in the Pop II component of the model, but also due to degeneracies between the Pop III model parameters.

From Fig. 6, we can see some of these degeneracies already. The size of each green polygon in the top row of Fig. 6 is set by the

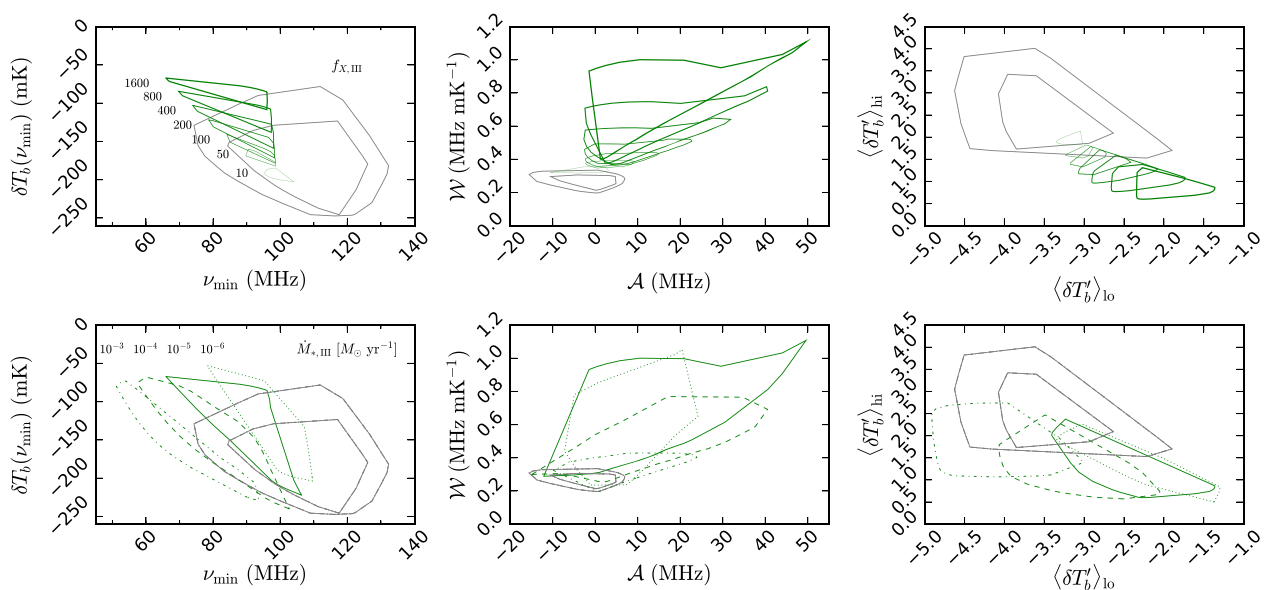


Figure 6. Comparison of Pop II and Pop III models in three diagnostic spaces, including the position of the absorption trough (left), the prominence of its wings and its asymmetry (middle), and the mean slopes at frequencies above and below the extremum (right), as in Fig. 4. Black contours enclose sets of Pop II models (identical to those in Fig. 4), while the green polygons are slices through our Pop III model grid, first assuming $\dot{M}_{*,\text{III}} = 10^{-5} M_{\odot} \text{ yr}^{-1}$ and select $f_{X,\text{III}}$ values (top row), and then for a set of $\dot{M}_{*,\text{III}}$ values having ‘marginalized’ over all $f_{X,\text{III}}$ (bottom row). Measurements falling in regions of overlap between the green and black contours would have no clear evidence of Pop III, while measurements falling only within the green contours would be suggestive of Pop III.

range of \mathcal{T}_c and \mathcal{E}_c values we explore, and thus give some indication of the signal’s sensitivity to the details of the Pop III SFRD at fixed $f_{X,\text{III}}$ and $\dot{M}_{*,\text{III}}$. As a reminder, with $\dot{M}_{*,\text{III}} = 10^{-5} M_{\odot} \text{ yr}^{-1}$, the peak SFRD in our $(\mathcal{T}_c, \mathcal{E}_c)$ grid varies by only a factor of ~ 10 , while $6 \lesssim z_{\text{max}} \lesssim 25$. As a result, measurements with error bars of order the size of the green polygons are probing the peak Pop III SFRD at the order of magnitude level.

However, there is also significant overlap between the polygons in the right two columns of Fig. 6, which indicates the degeneracy between the Pop III SFRD and $f_{X,\text{III}}$. Though the green polygons in the upper left panel of Fig. 6 are distinct, one must remember that each adopts the same value for $f_{X,\text{III}}$. As a result, differentiating the effects of $f_{X,\text{III}}$ from the detailed shape of the Pop III SFRD will require additional constraints.

The results presented in this section so far have adopted $\dot{M}_{*,\text{III}} = 10^{-5} M_{\odot} \text{ yr}^{-1}$. Boosting this parameter will of course affect the Pop III SFRD, making the signature of Pop III stronger, at least in the $\delta T_b(\nu_{\text{min}})$ plane, which most intuitively responds to amplification of the SFRD. In the bottom row of Fig. 6, we explore the effects of $\dot{M}_{*,\text{III}}$. For $\dot{M}_{*,\text{III}} = 10^{-4} M_{\odot} \text{ yr}^{-1}$ (dashed), most Pop III models now have troughs that are distinct from the refined set of Pop II models (i.e., the inner polygon), while $\dot{M}_{*,\text{III}} = 10^{-3} M_{\odot} \text{ yr}^{-1}$ (dotted) makes Pop III distinct even for the more conservative, complete set of Pop II-only models. Alternatively, increasing $\dot{M}_{*,\text{III}}$ reduces the signature in (A, W) space (lower middle panel) and in the derivative of the signal (lower right panel), though each metric retains at least some sensitivity to Pop III. Note that these scenarios may be quite extreme, as they require the formation of tens or hundreds of $\sim 100 M_{\odot}$ stars per Pop III halo every 10 Myr (for further discussion, see Section 4.2).

3.3 Side effects of persistent Pop III star formation

If Pop III stars keep forming until late times, they may measurably influence – and perhaps violate – pre-existing constraints. To

address this concern, in this section we focus on whether global 21-cm spectra with strong signatures of Pop III cause tension with current limits on the reionization history and the $z = 0$ cosmic X-ray background intensity.

So far, in order to isolate the effects of heating and ionization, we have assumed that the escape fraction of Lyman-continuum photons is zero for Pop III haloes. However, some simulations predict that LyC escape fractions can be a strong function of halo mass (though this is likely sensitive to resolution; Ma et al. 2015), rendering Pop III haloes a potentially important source population to consider for reionization (e.g., Wise & Cen 2009). However, star formation rates in minihaloes may be low enough to counteract large escape fractions, confining their effects to the earliest stages of reionization (Xu et al. 2016), thus rendering them unimportant to the bulk of the process (Kimm et al. 2017).

Adopting our default model, that assumes massive Pop III stars that form at a rate $\dot{M}_{*,\text{III}}$, we investigate the impact of increasing on the cosmic microwave background (CMB) optical depth, τ_e , in Fig. 7. For our default Pop II-only model with $f_{\text{esc,II}} = 0.1$, the addition of Pop III stars that form only for a short time in high- z haloes (solid blue) affects τ_e negligibly, even if $f_{\text{esc,III}} = 1$. The corresponding SFRD of this model is identical to the solid blue line in the upper right panel of Fig. 2. If we instead assume $\mathcal{T}_c = 250$ Myr and $\mathcal{E}_c = 10^{53}$ erg, Pop III star formation is much more plentiful at late times, driving τ_e outside the preferred *Planck* 2- σ range if $f_{\text{esc,III}} \gtrsim 0.4$ (dotted magenta). In between, e.g., if $\mathcal{T}_c = 25$ Myr and $\mathcal{E}_c = 10^{52}$ erg, $f_{\text{esc,III}} = 1$ is still allowed at the 2σ level.

These results are again driven by our adoption of parameters consistent with massive $\sim 100 M_{\odot}$ stars, which emit $N_{\text{ion}} \sim 10^5$ ionizing photons per stellar baryon. If the Pop III IMF is more normal, and N_{ion} is reduced to values of $5\text{--}10 \times 10^3$, as is appropriate even for metal-poor Pop II sources, then Pop III sources will have a negligible impact on τ_e unless they form at rates substantially higher than $\dot{M}_{*,\text{III}} = 10^{-5} M_{\odot} \text{ yr}^{-1}$. Though difficult to compare closely, this is roughly in agreement with Visbal et al. (2015) and Sun &

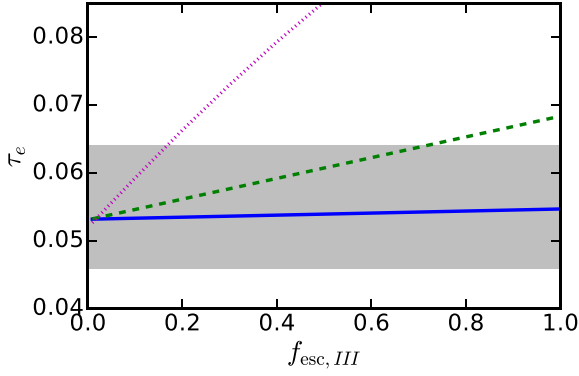


Figure 7. CMB optical depth as a function of Pop III LyC escape fraction, holding the Pop II escape fraction fixed at $f_{\text{esc}} = 0.1$. Solid, dashed, and dotted curves assume increasingly persistent Pop III star formation, from $\mathcal{T}_c = 2.5$ Myr and $\mathcal{E}_c = 10^{51}$ erg (solid), to $\mathcal{T}_c = 250$ Myr and $\mathcal{E}_c = 10^{53}$ erg, with $\dot{M}_{*,\text{III}} = 10^{-5} M_{\odot} \text{ yr}^{-1}$. For reference, the exact set of corresponding SFHs and global 21-cm spectra are shown in the upper-right panels of Fig. 2 and 3. 68 per cent confidence interval from Planck Collaboration et al. (2016b) is shown in grey.

Furlanetto (2016). Similarly, only in our most extreme models do Pop III stars produce a substantial tail in the reionization history. For example, even for our intermediate case (dashed green curve in Fig. 7) with $f_{\text{esc,III}} = 1$, the volume-averaged ionization fraction is only ~ 10 per cent at $z = 15$, within the limits presented in Miranda et al. (2017).

Next, because Pop III sources are most noticeable in the global 21-cm signal when their X-ray production efficiencies are high $f_{X,\text{III}} \gg 1$, we investigate whether such scenarios violate constraints on the $z = 0$ X-ray background intensity. To do so, we extract the cosmic X-ray background spectrum at $z = 6$ (when our calculations terminate) and evolve the background to $z = 0$ assuming no attenuation by the IGM. This is a reasonable assumption since the $z = 0$ soft X-ray background (typically defined as the 0.5–2 keV band) probes rest-frame photon energies of 3.5–14 keV at $z = 6$, which will be optically thin even to dense absorbers in the IGM until relatively late times.

In our default case of a pure MCD X-ray spectrum, there is relatively little emission at high energies $\gtrsim 10$ keV, which will artificially bias our predictions for the $z = 0$ CXRB low. To explore a more realistic case, we instead use the SIMPL model (Steiner et al. 2009) as our input X-ray spectrum, and assume that a fraction $f_{\text{sc}} = 0.1$ of accretion disk photons are up-scattered to a high energy tail, in which emission follows a power-law of index α_X . The introduction of these modifications has a very minor effect on the thermal history. As a result, one can compare models for the global signal and CXRB at fixed $f_{X,\text{III}}$ at the level of ~ 10 mK and \sim few MHz in the location of the absorption trough (see figs 4 and 5 of Mirocha 2014).

In Fig. 8, we find that Pop III sources alone provide an essentially negligible contribution to the $z = 0$ CXRB, unless $f_{X,\text{III}} \gtrsim 10^3$ and $\dot{M}_{*,\text{III}} \gg 10^{-5} M_{\odot} \text{ yr}^{-1}$. This is a corner of parameter space that is perhaps unreasonable theoretically, as it requires extremely efficient Pop III star formation, which can likely only occur if the IMF is fairly normal. But, if the IMF is normal, values of $f_{X,\text{III}} \sim 10^3$ are much more difficult to explain. We will discuss this further in Section 4.2.

Notice that all curves approach $j_{\text{sxrb}} \sim 10^{-15} \text{ erg s}^{-1} \text{ cm}^{-2} \text{ Hz}^{-1} \text{ deg}^{-2}$ when $f_{X,\text{III}}$ is small. This is the CXRB intensity produced in our default model from Pop

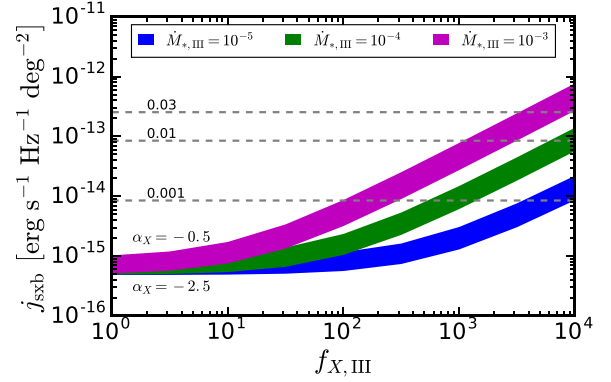


Figure 8. Cosmic X-ray background intensity at $z = 0$ generated by our models as a function of $f_{X,\text{III}}$ (x-axes) and $\dot{M}_{*,\text{III}}$ (coloured bands). The width of each band corresponds to a difference in the assumed high energy power-law index, α_X , as indicated in the lower left portion of the plot. We assume our default Pop II model with $f_{\text{sc}} = 0.1$ and $\alpha_X = -2.5$, which sets the floor at $10^{-15} \text{ erg s}^{-1} \text{ cm}^{-2} \text{ Hz}^{-1} \text{ deg}^{-2}$. Dashed lines indicate fluxes at a fixed fraction of the Cappelluti et al. (2012) measurement of the 0.5–2 keV CXRB flux at $z = 0$. The Cappelluti et al. (2012) models find that the unresolved fraction is $\lesssim 3$ per cent, meaning our modelled Pop III sources are only in tension with the CXRB if $f_{X,\text{III}} \gtrsim 10^3$ and $\dot{M}_{*,\text{III}} \gtrsim 10^{-3} M_{\odot} \text{ yr}^{-1}$.

II sources only (i.e., roughly 0.01 per cent of the unresolved background). If we have underestimated the contribution of Pop II galaxies to the present day CXRB by a factor of 10 or 100, this will raise the floor in j_{sxrb} in Fig. 8, leaving less room for Pop III sources. Any further observational reduction in the unresolved fraction would similarly limit $f_{X,\text{III}}$ to smaller values. If that reduction were due to low redshift sources only, it could help improve lower limits on the strength of the global 21-cm absorption signal (Fialkov et al. 2017).

To summarize, it appears that strong signatures of Pop III stars in the global 21-cm signal can arise without violating pre-existing limits on τ_e or j_{sxrb} . This could be subject to revision if either the UV or X-ray backgrounds generated by Pop II sources are much stronger (and/or harder) than is assumed in our default model, or if more of τ_e and the unresolved fraction can be attributed to normal star-forming galaxies.

4 DISCUSSION

We have found that massive Pop III stars can give rise to broad, asymmetric wings in the global 21-cm signal that do not arise in Pop II-only models. While such sources also affect the position of the absorption minimum, uncertainties in the properties of Pop II sources could prevent an unambiguous detection of Pop III based on the trough position alone. In this section, we focus on the observational implications of these findings, as well as so-far-neglected elements of the theoretical modelling that, if treated explicitly, could lead to ambiguity in the interpretation of the signal's shape.

4.1 Implications for Global 21-cm experiments

By construction, our results agree with those of Mirocha et al. (2017) in that our most ‘vanilla’ models for the global 21-cm signal predict a strong absorption trough near ~ 100 MHz. Though adding a Pop III component to the model can dramatically suppress the amplitude of the absorption signal, its location in frequency remains

largely unaffected unless Pop III star formation is very efficient ($\gtrsim 10^4 M_\odot$ per event). The critical finding in this work is that shallow absorption troughs driven by Pop III sources are *not* accompanied by strong emission features at high frequencies, which leads to an asymmetry in the width of the trough. This is in contrast to scenarios in which Pop II sources dominate the X-ray background at all epochs, in which case shallow troughs are accompanied by strong emission signals since the Pop II SFRD is monotonically rising as reionization progresses, and the X-ray emission is assumed to trace star formation. In these cases, the global 21-cm signal remains relatively symmetrical ($|A| \lesssim 5 - 10$ MHz).

While most forecasting work has focused on the ability of various experimental setups to constrain the locations of extrema in the global 21-cm signal (e.g., Pritchard & Loeb 2010; Harker et al. 2012; Liu et al. 2013; Harker et al. 2016), and perhaps the width of the absorption trough (Presley, Liu & Parsons 2015; Bernardi, McQuinn & Greenhill 2015), to our knowledge there has been no investigation of the information content of the trough’s symmetry or prospects for its characterization. We suspect that recovery of shape information will, in general, be more difficult than recovery of the ‘turning points,’ especially for the Pop III models, whose shallow late-time gradients will increase their resemblance to the galactic foreground.

Though the asymmetry has not been quantified in previous works, Cohen et al. (2017) investigated the mean slope between the minimum and maximum of the signal in a set of semi-numeric models and found $1 \gtrsim \langle \delta T'_b \rangle / (\text{mK MHz}^{-1}) \gtrsim 6$. Our Pop II-only models span a narrower range, $1.5 \gtrsim \langle \delta T'_b \rangle \gtrsim 3$, while our Pop III models exhibit $\langle \delta T'_b \rangle \lesssim 1.5$ mK MHz $^{-1}$ (see Fig. 4). It is challenging to make a direct comparison given the difference in methods, but it is at least encouraging to see that the Cohen et al. (2017) models rarely produce realizations with $\langle \delta T'_b \rangle \lesssim 2$ mK MHz $^{-1}$, since there was no attempt to treat Pop III sources in detail in their work.

Observational efforts have recently commenced attempts to rule out ‘cold reionization’ scenarios (Monsalve et al. 2017; Singh et al. 2017), which have the potential to produce the strongest absorption signals. In our framework, they should be treated as the null hypothesis, as one arrives at strong late-peaking absorption signals when constructing minimal models of high- z galaxies. In some sense, simply ruling these models out may provide the first evidence of ‘new’ source populations at high- z . However, such claims require high confidence in the Pop II SFRD (and its extrapolation) and L_X -SFR relation of Pop II galaxies at high- z .

Future data analysis pipelines could call our models directly and attempt to fit for the parameters of Pop II and Pop III sources. Even for simple models like ours, this can be fairly expensive, and may also be somewhat restricting since our models cannot fit an arbitrary signal. In practice, it may be more economical to use a flexible parametric form for the signal that is capable of generating a wide variety of realizations, and simply compute \mathcal{A} and \mathcal{W} in post-processing. A crude form of model selection could then be applied simply by asking whether or not the best-fitting value is consistent with Pop II-only models (using, e.g., our contours in Figs 4-6), or if an additional component is required.

Should the calibration of the Pop II component of the model mature in the coming years, precise measurements may be able to move beyond a simple null test and attempt to constrain the parameters of the Pop III model. We defer a detailed forecast of this possibility to future work.

Finally, before concluding, we reconsider the possibility that the true global 21-cm signal qualitatively differs from the Mirocha et al.

(2017) predictions of a strong, high-frequency trough (Section 4.2), and comment on effects that we have neglected that could potentially induce asymmetry in the global 21-cm signal, and thus provide a source of confusion in future studies (Section 4.3).

4.2 Implications of dramatic departures from ~ 100 MHz troughs

In Mirocha et al. (2017), we suggested that observational rejections of our models would most likely indicate the need for ‘new’ source populations – i.e., those deviating strongly from the inferred (or extrapolated) properties of high- z galaxies. Given that we explicitly neglected star-formation in minihaloes, such an outcome would not spell disaster for galaxy formation models, but only serve to emphasize the importance of very low-mass objects in the early Universe. Having since added low-mass haloes in a physically motivated way, our predictions for the amplitude of the absorption trough cover a broader range, though it is still difficult to achieve low-frequency absorption troughs. What would the implications of a $\nu_{\min} \ll 100$ MHz absorption trough mean *now*?

In order to produce realizations with early troughs, we need to revise the model in one or more of the following ways:

- (i) Allow massive Pop III stars to form in large numbers (tens or hundreds per 10 Myr; our $\dot{M}_{*,\text{III}} > 10^{-5} M_\odot \text{ yr}^{-1}$ cases), as explored in Figs 2 (bottom two rows) and 6.
- (ii) Turn off global LW feedback, which keeps M_{\min} at low levels and boosts the abundance of Pop III star-forming haloes as a result.
- (iii) Introduce a floor in the Pop II star formation efficiency so that when Pop III haloes transition to Pop II, their SFE is much larger than extrapolation of our default double power-law SFE would predict, leading to a stronger UV background capable of triggering Wouthuysen-Field coupling earlier.
- (iv) A strong, but globally short-lived epoch of Pop III star formation, that can induce a second trough at low frequencies $\nu \sim 50 - 60$ MHz. Though the typical trough would still occur at higher frequencies, the ‘dramatic’ designation still seems appropriate.

Let us entertain each of these possibilities in turn.

First, the formation of massive $\sim 100 M_\odot$ Pop III stars in large numbers ($\dot{M}_{*,\text{III}} > 10^{-5} M_\odot \text{ yr}^{-1}$) may be physically unrealistic. For example, it seems unlikely that the small haloes could recover quickly from such dramatic bursts of star formation, which are almost surely accompanied by many supernovae¹³. Long recovery times could thus counteract intense star formation episodes, keeping $\dot{M}_{*,\text{III}}$ at low, relatively constant, levels.

One way around this is to assume that the Pop III IMF is at least somewhat normal, in which case the effects of supernovae feedback on the galactic gas supply could be reduced and recovery times might remain short, even in the face of $\sim 10^3$ or $10^4 M_\odot$ star-forming events. However, changing the IMF in this way also reduces the strength of the UV background by a factor of $\sim 5 - 10$, since low-mass stars produce UV photons less efficiently than very massive stars. As a result, the impact of such a population on the low-frequency part of the global 21-cm signal will also be reduced. In order to shift the absorption trough to low frequencies (as in the bottom two rows of Fig. 2), one would need to enhance $\dot{M}_{*,\text{III}}$ by an extra factor of $\sim 5 - 10$ more than the values quoted along the edge of Fig. 2.

¹³Unless most or all Pop III stars undergo direct collapse to a black hole.

Furthermore, if the Pop III IMF is normal, it might be difficult to justify $f_{X,\text{III}} \gg 10$ following the arguments of equations (3)–(4), further reducing the impact of such sources on the global 21-cm signal unless $M_{*,\text{III}}$ is very large ($\gtrsim 10^{-3}$). These arguments support the Pop II-only predictions of Mirocha et al. (2017), which favour an absorption trough at relatively high frequencies, $\nu_{\text{min}} \sim 100$ MHz. Clearly, as we have shown, Pop III stars can modify the amplitude of the trough, though substantially altering its frequency – and recovering models with ~ 70 MHz troughs (as have been common in recent years; Furlanetto 2006; Pritchard & Loeb 2010; Mirocha, Harker & Burns 2015) – may require unreasonably efficient Pop III star formation. Fortunately, the asymmetry (though perhaps subtle), appears to emerge even if both the efficiency of Pop III star formation and $f_{X,\text{III}}$ are relatively small.

Pop III IMF effects aside, low-frequency troughs may also arise if global LW feedback is weaker than expected, or non-existent. One way to reduce (or eliminate) feedback is to explicitly treat the interplay between the UV and X-ray backgrounds. Because X-rays are able to travel through dense proto-stellar clouds, they can boost the free electron fraction upon absorption and thus catalyse the formation rate of H_2 and fend off the destruction of H_2 by LW photons (Machacek et al. 2003; Glover 2016; Ricotti 2016). The resultant decline in $M_{\text{min,III}}$ permits Pop III star formation in haloes of lower mass than the usual relation between J_{LW} and $M_{\text{min,III}}$ would suggest, enhancing the Pop III SFRD, and thus all radiation backgrounds generated by Pop III sources.

Next, though there is some indication that the slope of the Pop II star formation efficiency may become more shallow at low mass (Mason et al. 2015), we can think of no obvious reason why Pop II haloes would have a minimum star formation efficiency. Continued efforts to measure the galaxy luminosity function at higher redshifts and fainter magnitudes should help explore this possibility in the coming years.

Finally, a single ~ 100 MHz trough could be accompanied by another trough at low frequencies, which in our model occurs only in situations of very efficient, though globally brief (i.e., $z \gtrsim 20$ only), Pop III star formation. This only happens if the transition to Pop II occurs at a fixed halo binding energy, though this is somewhat unphysical, as passage through a critical binding energy does not influence the cooling properties of gas in a halo. However, it is possible for haloes to skip the *massive* Pop III phase via a different mechanism: arrival at the atomic-cooling threshold before forming their first stars. In this case, cooling is expected to be efficient (Susa et al. 1998; Nakamura & Umemura 2002; Oh & Haiman 2002), and lead to a stellar IMF less top-heavy than that which arises in molecular-cooling haloes, though the stars are still technically Pop III as they have zero metallicity. This has led to a distinction between Pop III.1 stars (born in molecular-cooling haloes) and Pop III.2 stars (born in atomic-cooling haloes, or from previously ionized gas).

Mebane et al. (2017) showed that many haloes can skip the Pop III phase if the minimum mass rises rapidly at early times, which is easiest to achieve if the Pop II SFRD is high at early times (since Pop II haloes do not ‘feel’ LW feedback). As a result, this could be related to our previous point, regarding the potential for a shallower Pop II SFE, which would boost the Pop II SFRD at early times. Short of introducing these kinds of stars as a new source population in our model, it is most sensible to count this as Pop II star formation, since the LW and X-ray yields would be less extreme for these haloes than the molecular cooling haloes in the Pop III phase. As a result, their impact on the global 21-cm signal (and PISN supernova rates, for that matter), will be fairly minimal.

While drawing a distinction between the Pop III.1 and Pop III.2 sources may have important consequences for the global 21-cm signal, we note that the predicted Pop III SFRD in this scenario in Mebane et al. (2017) is small ($\sim 10^{-6} M_{\odot} \text{ yr}^{-1} \text{ cMpc}^{-3}$ at peak), compared to the $\gtrsim 10^{-5} M_{\odot} \text{ yr}^{-1} \text{ cMpc}^{-3}$ realizations that led to a double trough in this study (see Fig. 2). Furthermore, because of the efficient Pop II star formation, the Ly- α background would be strong and rise monotonically with time, thus preventing the emergence of a double trough. Rejection of the double trough scenario observationally may thus be capable of ruling out a very specific – though unlikely – set of circumstances in high- z star-forming galaxies.

4.3 Potential for confusion

In the previous section, we focused on effects that could push the absorption minimum to low frequencies, beyond what we can comfortably accomplish within the confines of our LF-calibrated models. In this section, we focus instead on the possibility of more subtle effects that we have yet to include that may weaken our central claims.

To phrase our results very conservatively, broad asymmetric wings in the global 21-cm signal are indicative of a slowly rising (or flat) heating rate density at high- z . It seems natural to associate this with Pop III star-forming haloes, since numerous studies have predicted shallow Pop III SFRDs, and thus luminosity densities at all wavelengths. But, there could be other mechanisms at work, either on the Pop II or Pop III side of the model, that could complicate such expectations.

For example, a source population that only emits X-rays at early times, or produces X-rays at a very gradual rate, could mimic the signature of our Pop III model. Dark matter annihilation may provide such a source, as the heating rates in most models evolve very gradually with redshift (e.g., Valdes et al. 2013; Lopez-Honorez et al. 2016). We plan to address this potential source of confusion in future work.

We have also neglected emission from super-massive black holes, whose growth rate may not mirror the growth rates of galaxies at early times, and could thus generate radiation backgrounds that are decoupled from the cosmic SFRD. However, heating rates from rapidly growing stellar remnants and direct collapse BHs are both still expected to be quite steep in redshift (Tanaka, O’Leary & Perna 2016). If such predictions hold, neglect of such sources may bias inferred values of the SFRD and f_X values for Pop II and Pop III sources, but would be unlikely to introduce much asymmetry to the signal.

More mundane source of gradual heating, i.e., those which originate in ‘normal’ galaxies, are perhaps more difficult to imagine since they require that the galaxy population become a less efficient producer of X-rays *per unit star formation* on time-scales shorter than ~ 1 Gyr. Only then can the rapid rise in the Pop II SFRD be offset to produce a gradual heating rate.

For example, because X-ray production likely becomes less efficient with increased metallicity, which ought to rise monotonically in galaxies with time, one might think this a reasonable way to generate gradual heating without Pop III sources. However, the Pop II SFRD is expected to rise by ~ 3 orders of magnitude over $6 \lesssim z \lesssim 20$, whereas L_X/SFR only appears to decline by a factor of ~ 10 between $Z = 10^{-3}$ and solar metallicity (Brorby et al. 2016). As a result, rapid evolution in the properties of X-ray binaries is unlikely to be able to counteract the rapid rise in the SFRD.

5 CONCLUSIONS

Our main results can be summarized as follows:

(i) Pop III stars can affect the global 21-cm signal through both their UV and X-ray emissions. Because the Pop III SFRD flattens, and sometimes declines before reionization is complete, boosts in the LW and X-ray backgrounds (relative to the Pop II-only case) occur mostly at the highest redshifts, and thus mostly affect the low-frequency portion of the global 21-cm signal. This leads to broad absorption troughs skewed towards high frequencies.

(ii) We explore two ways to quantify this modulation of the signal: the asymmetry, \mathcal{A} , and the prominence of the wings of the signal, \mathcal{W} , both of which seem to clearly identify the presence of Pop III sources, even in cases where the trough position is consistent with a Pop II-only model.

(iii) These models reinforce the Mirocha et al. (2017) predictions, since Pop III star formation must be extremely efficient to drive the signal to frequencies below ~ 90 MHz. Fortunately, the signature of Pop III – albeit subtle – appears even in the likely event that their overall SFRD is small. Its measurement will rely entirely on the fidelity of signal–foreground separation. Efforts to understand the extent to which such a measurement is possible are underway.

The authors thank the anonymous referee for a very helpful report. This work was supported by the National Science Foundation through awards AST-1440343 and 1636646, by NASA through award NNX15AK80G, and was completed as part of the University of California Cosmic Dawn Initiative. In addition, this work was directly supported by the NASA Solar system Exploration Research Virtual Institute cooperative agreement number 80ARC017M0006. We acknowledge support from the University of California Office of the President Multicampus Research Programs and Initiatives through award MR-15-328388. KS gratefully acknowledges support from NSF Grant PHY-1460055 through the UCLA Physics & Astronomy REU program. DT acknowledges support from the University of California’s Leadership Excellence through Advanced DegreeS (UC LEADS) program. This work used computational and storage services associated with the Hoffman2 Shared Cluster provided by UCLA Institute for Digital Research and Education’s Research Technology Group.

Software: PYTHON, and packages MATPLOTLIB, NUMPY, SCIPY, DESCARTES, and SHAPELY.

REFERENCES

- Abel T., Bryan G. L., Norman M. L., 2002, *Science*, 295, 93
 Belloni T. M., 2010, in Belloni T., ed., *Lecture Notes in Physics*, Berlin Springer Verlag, 794, 53
 Bernardi G., McQuinn M., Greenhill L. J., 2015, *ApJ*, 799, 90
 Bernardi G. et al., 2016, *MNRAS*, 461, 2847
 Bouwens R. J. et al., 2015, *ApJ*, 803, 34
 Bowler R. A. A. et al., 2017, *MNRAS*, 469, 448
 Bowman J. D., Rogers A. E. E., 2010, *Nat*, 468, 796
 Bowman J. D. et al., 2018, *Nature*, 555, 67
 Bromm V., 2013, *Rep. Progr. Phys.*, 76, 112901
 Bromm V., Loeb A., 2003, *Nature*, 425, 812
 Bromm V., Coppi P. S., Larson R. B., 1999, *ApJL*, 527, L3
 Bromm V., Kudritzki R. P., Loeb A., 2001, *ApJ*, 552, 464
 Brorby M. et al., 2016, *MNRAS*, 457, 4081
 Burns J. O. et al., 2012, *Adv. Space Res.*, 49, 433
 Burns J. O. et al., 2017, *ApJ*, 844, 33
 Cappelluti N. et al., 2012, *MNRAS*, 427, 651
 Chen X., Miralda-Escudé J., 2004, *ApJ*, 602, 1
 Chluba J., Thomas R. M., 2011, *MNRAS*, 412, 748
 Chuzhoy L., Alvarez M. A., Shapiro P. R., 2006, *ApJ*, 648, L1
 Cohen A. et al., 2017, *MNRAS*, 472, 1915
 Cooke J. et al., 2012, *Nature*, 491, 228
 Das A. et al., 2017, *MNRAS*, 469, 1166
 Eldridge J. J., Stanway E. R., 2009, *MNRAS*, 400, 1019
 Fialkov A. et al., 2012, *MNRAS*, 424, 1335
 Fialkov A. et al., 2014, *MNRAS*, 437, L36
 Fialkov A. et al., 2017, *MNRAS*, 464, 3498
 Field G. B., 1958, *Proc. IRE*, 46, 240
 Finkelstein S. L. et al., 2015, *ApJ*, 810, 71
 Fragos T. et al., 2013, *ApJ*, 776, L31
 Fukugita M., Kawasaki M., 1994, *MNRAS*, 269, 563
 Furlanetto S. R., 2006, *MNRAS*, 371, 867
 Furlanetto S. R., Johnson Stoeve S., 2010, *MNRAS*, 404, 1869
 Furlanetto S. R., Pritchard J. R., 2006, *MNRAS*, 372, 1093
 Furlanetto S. R. et al., 2017, *MNRAS*, 472, 1576
 Glover S. C. O., 2016, astro-ph/1610.05679
 Haiman Z., Rees M. J., Loeb A., 1997, *ApJ*
 Harker G. J. A. et al., 2012, *MNRAS*, 419, 1070
 Harker G. J. A. et al., 2016, *MNRAS*, 455, 3829
 Heger A., Woosley S. E., 2002, *ApJ*, 567, 532
 Hirano S. et al., 2014, *ApJ*, 781, 60
 Hirata C. M., 2006, *MNRAS*, 367, 259
 Hosokawa T. et al., 2011, *Science*, 334, 1250
 Jaacks J. et al., 2018, *MNRAS*, 475, 4396
 Jeon M. et al., 2014, *MNRAS*, 444, 3288
 Jeon M., Besla G., Bromm V., 2017, *ApJ*, 848, 85
 Keller S. C. et al., 2014, *Nat*, 506, 463
 Kimm T. et al., 2017, *MNRAS*, 466, 4826
 Lewis A., Challinor A., Lasenby A., 2000, *ApJ*, 538, 473
 Liu A. et al., 2013, *Phys. Rev. D*, 87, 043002
 Lopez-Honorez L. et al., 2016, *JCAP*, 8, 004
 Ma X. et al., 2015, *MNRAS*, 453, 960
 Machacek M. E., Bryan G. L., Abel T., 2003, *MNRAS*, 338, 273
 Madau P., Meiksin A., Rees M. J., 1997, *ApJ*, 475, 429
 Magg M. et al., 2018, *MNRAS*, 473, 5308
 Mason C. A., Trenti M., Treu T., 2015, *ApJ*, 813, 21
 Matthee J. et al., 2017, *ApJ*, 851, 145
 McBride J., Fakhouri O., Ma C.-P., 2009, *MNRAS*, 398, 1858
 McQuinn M., O’Leary R. M., 2012, *ApJ*, 760, 3
 Mebane R. H., Mirocha J., Furlanetto S. R., 2017, astro-ph/1602.08065
 Mesinger A., Furlanetto S., Cen R., 2011, *MNRAS*
 Mesinger A., Greig B., Sobacchi E., 2016, *MNRAS*, 459, 2342
 Mineo S., Gilfanov M., Sunyaev R., 2012, *MNRAS*, 419, 2095
 Mirabel I. F. et al., 2011, *A&A*, 528, A149
 Miranda V. et al., 2017, *MNRAS*, 467, 4050
 Mirocha J., 2014, *MNRAS*, 443, 1211
 Mirocha J., Furlanetto S. R., 2018, astro-ph/1803.03272
 Mirocha J., Harker G. J. A., Burns J. O., 2015, *ApJ*, 813, 11
 Mirocha J., Furlanetto S. R., Sun G., 2017, *MNRAS*, 464, 1365
 Mitsuda K. et al., 1984, *PASJ*, 36, 741
 Monsalve R. A. et al., 2017, *ApJ*, 847, 64
 Murray S. G., Power C., Robotham A. S. G., 2013, *Astron. Comput.*, 3, 23
 Nakamura F., Umemura M., 2002, *ApJ*, 569, 549
 Naoz S., Barkana R., 2007, *MNRAS*, 377, 667
 O’Shea B. W., Norman M. L., 2007, *ApJ*, 654, 66
 O’Shea B. W. et al., 2005, *ApJ*, 628, L5
 O’Shea B. W. et al., 2015, *ApJL*, 807, L12
 Oh S. P., Haiman Z., 2002, *ApJ*, 569, 558
 Patra N. et al., 2015, *ApJ*, 801, 138
 Planck Collaboration et al., 2016a, *A&A*, 594, A13
 Planck Collaboration et al., 2016b, *A&A*, 596, A107
 Postnov K. A., 2003, *Astron. Lett.*, 29, 372
 Presley M. E., Liu A., Parsons A. R., 2015, *ApJ*, 809, 18
 Pritchard J. R., Furlanetto S. R., 2006, *MNRAS*, 367, 1057
 Pritchard J. R., Loeb A., 2010, *Phys. Rev. D*, 82, 23006
 Ricotti M., 2016, *MNRAS*, 462, 601
 Schaerer D., 2002, *A&A*, 382, 28

- Shaver P. A. et al., 1999, *A&A*, 345, 380
 Sheth R. K., Mo H. J., Tormen G., 2001, *MNRAS*, 323, 1
 Singh S. et al., 2017, *ApJL*, 845, L12
 Smith B. D. et al., 2015, *MNRAS*, 452, 2822
 Sobral D. et al., 2015, *ApJ*, 808, 139
 Sokolowski M. et al., 2015, *PASA*, 32, e004
 Steiner J. F. et al., 2009, *PASP*, 121, 1279
 Sun G., Furlanetto S. R., 2016, *MNRAS*, 460, 417
 Susa H. et al., 1998, *Progr.Theor. Phys.*, 100
 Tanaka T. L., O’Leary R. M., Perna R., 2016, *MNRAS*, 455, 2619
 Tegmark M. et al., 1997, *ApJ*, 474, 1
 Trenti M., Stiavelli M., 2009, *ApJ*, 694, 879
 Tseliakhovich D., Hirata C., 2010, *PRD*, 82, 083520
 Tumlinson J., Shull J. M., 2000, *ApJ*, 528, L65
 Turk M. J., Abel T., O’Shea B., 2009, *Science*, 325, 601
 Valdes M. et al., 2013, *MNRAS*, 429, 1705
 Verner D. A., Ferland G. J., 1996, *ApJS*, 103, 467
 Visbal E. et al., 2014, *MNRAS*, 445, 107
 Visbal E., Haiman Z., Bryan G. L., 2015, *MNRAS*, 453, 4456
 Voytek T. C. et al., 2014, *ApJL*, 782, L9
 Whalen D. J. et al., 2014, *ApJ*, 781, 106
 Wise J. H., Cen R., 2009, *ApJ*, 693, 984
 Wouthuysen S. A., 1952, *AJ*, 57, 31
 Xu H. et al., 2016, *ApJ*, 833, 84
 Zygelman B., 2005, *ApJ*, 622, 1356

This paper has been typeset from a \TeX/L\AA\TeX file prepared by the author.